On the diurnal cycle of deep convection, high-level cloud and upper troposphere water vapor in the Multi-scale Modeling Framework

Yunyan Zhang,[1] Stephen A. Klein,[1] Chuntao Liu,[2] Baijun Tian,[3] Roger T. Marchand,[4] John M. Haynes,[5] Renata B. McCoy,[1] Yuying Zhang,[1] Thomas P. Ackerman[4]

Yunyan Zhang, Atmospheric, Earth & Energy Division, Lawrence Livermore National Laboratory, L-103, P.O. Box 808, Livermore, CA 94551, USA. (zhang25@llnl.gov)

[1]Lawrence Livermore National Laboratory,
Livermore, California, USA.

[2]Department of Meteorology,
University of Utah, Salt Lake City, Utah, USA.

[3]Joint Institute for Regional Earth System Science and Engineering,
University of California, Los Angeles, CA, USA.

[4]Joint Institute for the Study of the Atmosphere and Ocean, University of Washington,
Seattle, Washington, USA.

[5]Department of Atmospheric Science, Colorado State University, Fort Collins, Colorado, USA.

Abstract. The Multi-scale Modeling Framework (MMF, also called "super-parameterization") embeds a cloud resolving model (CRM) at each grid column of a general circulation model to replace traditional parameterizations of moist convection and large-scale condensation. This study evaluates the diurnal cycle of deep convection, high-level clouds and upper troposphere water vapor by applying an infrared (IR) brightness temperature (T_b) and a precipitation radar (PR) simulator to the CRM column data. Simulator results are then compared with IR radiances from geo-stationary satellites and PR reflectivities from the Tropical Rainfall Measuring Mission (TRMM). While the actual surface precipitation rate in the MMF has a reasonable diurnal phase and amplitude when compared with TRMM observations, the IR simulator results indicate an inconsistency in the diurnal anomalies of high-level clouds between the model and the geo-stationary satellite data. Primarily due to its excessive high-level clouds, the MMF overestimates the simulated precipitation index (PI) and fails to reproduce the observed diurnal cycle phase relationships among PI, high-level clouds and upper troposphere relative humidity. The PR simulator results show that over the tropical oceans, the occurrence fraction of reflectivity in excess of 20 dBZ is almost one order of magnitude larger than the TRMM data especially at altitudes above 6 km. Both results suggest that the MMF oceanic convection is overactive and possible reasons for this bias are discussed. However, the joint distribution of simulated IR T_b and PR reflectivity indicates that the most intense deep con-

vection is found more often over tropical land than ocean, in agreements with previous observational studies.

1. Introduction

Climate modeling is a challenging and demanding task. Much of the uncertainty in predicting climate is attributed to cloud and cloud-related processes [*Arakawa*, 1975; *Houghton et al.*, 2001], which usually can not be resolved but are highly parameterized in general circulation models (GCMs). Improved representations of these processes are always at the heart of the model development and the effort has been ongoing for decades [*Arakawa*, 1969; *Randall et al.*, 2003]. Recently a key breakthrough, the Multiscale Modeling Framework (MMF, or "super-parameterization"), was proposed to solve the deadlocked situation on convection and cloud parameterizations in GCMs [*Grabowski and Smolarkiewicz*, 1999; *Grabowski*, 2001; *Khairoutdinov and Randall*, 2001; *Randall et al.*, 2003; *Khairoutdinov et al.*, 2005; *Tao et al.*, 2008]. In the MMF, a cloud resolving model (CRM) is implemented at each GCM grid column, replacing the traditional physics parameterizations for moist convection and large-scale condensation. Such an approach is a compromise in the pathway of climate modeling between "parameterize everything" and "resolve everything" [*Arakawa*, 2004; *Khairoutdinov et al.*, 2005].

Parallel to model development, a mandatory task is to make hand-in-hand evaluations to recognize the latest advances and to reveal remaining deficiencies. To correctly produce the diurnal cycle is one of the important measures in model evaluations [*Randall et al.*, 1991; *Yang and Slingo*, 2001; *Tian et al.*, 2004].

The diurnal cycles of deep convection and precipitation have been investigated intensively in observational studies with data from different platforms: rain gauges [*Gray and Jacobson*, 1977; *Dai et al.*, 1999] and weather reports [*Kraus*, 1963; *Dai*, 2001], ground-

based radar [*Short et al.*, 1997], satellite infrared sensors [*Short and Wallace*, 1980; *Soden et al.*, 2000; *Yang and Slingo*, 2001; *Tian et al.*, 2004], satellite microwave sensors [*Chang et al.*, 1995], and the precipitation radar on board the Tropical Rainfall Measuring Mission (TRMM) satellite [*Nesbitt and Zipser*, 2003; *Liu and Zipser*, 2008]. Most of these studies show that the deep convection and precipitation maxima occur most frequently in the early morning over open oceans and in the late afternoon/early evening over continents. Using geo-stationary satellite infrared radiances, *Tian et al.* [2004] demonstrated that the diurnal maximum of clear-sky upper troposphere relative humidity (UTH) lags the high-level cloud amount maximum, and that the latter lags the deep convection and precipitation maximum. Moreover using TRMM data, *Zipser et al.* [2006] and *Liu et al.* [2007] showed that extreme intense convection is found more often over land than ocean.

It is generally accepted that the diurnal late-afternoon/early-evening precipitation maximum over land is a thermodynamic response to the surface solar heating. While there is no consensus on the open ocean precipitation maximum in the early morning, three mechanisms have been proposed. The first involves the direct effects of radiation on cloud radiative heating: during the night (daytime), longwave radiative cooling (solar heating) enhances (inhibits) convection [*Kraus*, 1963; *Randall et al.*, 1991]. The second argues that the horizontal differential radiative cooling induces a diurnal variation in the divergence field, which results in greater low-level moisture convergence and precipitation in the early morning [*Gray and Jacobson*, 1977]. The third attributes the diurnal cycle to both the lifetime of large scale convective systems and a more complex interaction between clouds, radiation and near-surface thermodynamics [*Chen and Houze*, 1997; *Sui et al.*, 1997].

Several studies [*Khairoutdinov et al.*, 2005; *Wyant et al.*, 2006; *Ovtchinnikov et al.*, 2006; *Luo and Stephens*, 2006; *DeMott et al.*, 2007; *McFarlane et al.*, 2007; *Marchand et al.*, 2008] have compared the MMF with observations and traditional GCMs, such as the NCAR Community Atmosphere Model (CAM). Specifically *Khairoutdinov et al.* [2005] showed that relative to the CAM, the MMF improves the diurnal phase of non-drizzle precipitation frequency. In this paper, we investigate the diurnal variation of precipitation, deep convective and anvil clouds, and upper troposphere water vapor as well as the occurrence frequency of deep convection and updraft intensity.

In using a "model-to-satellite" approach [*Morcrette*, 1991; *Klein and Jakob*, 1999], we apply an infrared (IR) brightness temperature (T_b) [*Soden et al.*, 2000; *Tian et al.*, 2004] and a precipitation radar (PR) simulator (QuickBeam, *Haynes et al.* [2007]) to the MMF CRM column data to measure cloud condensate and precipitation, respectively. Simulator results are then compared with IR radiances from geo-stationary satellites [*Tian et al.*, 2004] and PR reflectivities from TRMM [*Zipser et al.*, 2006; *Liu et al.*, 2007]. In this study, we try to answer the following questions:

1. Is the MMF able to capture the diurnal cycle of deep convection, high-level clouds and the clear-sky UTH?

2. Is the MMF able to represent correctly the frequency and intensity of deep convection, particularly the land-sea contrast in the nature of deep convection?

In section 2, we detail the MMF simulations, observational datasets, and the simulators. The IR and PR simulator results are presented in section 3 and 4 respectively. In section 5, we examine the properties of deep convection and its land-sea contrast by considering the joint distribution of IR T_b and PR reflectivity. The results shown in section 3, 4 and 5

focus on the month of July. In the discussion section 6, we will show the results for January and address the uncertainties in the simulators and the factors that may be accountable for the model biases. A summary is presented in section 7.

2. The Model, observations and simulators

2.1. The MMF simulations

The MMF consists of two components: the parent GCM and the embedded CRM at each GCM grid column. The MMF simulation were conducted by Thomas Ackerman and Roger Marchand at the Pacific Northwest National Laboratory (now both at the University of Washington, Joint Center for the Study of Atmosphere and Ocean) using the model created by Khairoutdinov and Randall [*Khairoutdinov et al.*, 2005], except that the GCM — the NCAR CAM 3.0. [*Collins et al.*, 2006] — includes the finite-volume dynamical core instead of the semi-Lagrangian dynamical core.

CAM 3.0 is run with 26 vertical levels and a horizontal resolution of 2^o latitude and 2.5^o longitude. The CRM is the System for Atmospheric Modeling (SAM) [*Khairoutdinov and Randall*, 2003]. SAM is configured as a 2-dimensional CRM with 64 grid columns at each GCM grid, horizontally aligned along the east-west direction with 4 km spacing and cyclic lateral boundary conditions. It is run with 24 vertical levels, which are collocated with the lowest 24 levels in the parent GCM. Because the CRM resolves a distribution of clouds, radiation calculations are performed on each CRM grid column every 10 minutes. CAM and SAM are coupled every CAM time step, which is 20 minutes. The simulation is constrained by the observed monthly mean distributions of sea surface temperature and sea ice. The MMF simulation is initialized from a CAM restart and spans June 1998 to June 2002. In this simulation, 3 hourly "snap-shots" of the MMF CRM condensate and

water vapor fields along with more typical temporal and spatial averages of these fields were output at each of the GCM grid boxes.

In addition to the comparison between simulator results and observations, we also examine MMF's actual surface precipitation rate, high-level cloud amount, and upper tropospheric relative humidity without the use of a simulator in section 3 and 6.1. Surface precipitation rate is directly from MMF model output. A CRM column is defined high-cloudy if the cloud ice and water mixing ratio at any level above 400 hPa is larger than 0.01 g/kg. Upper tropospheric relative humidity is the layer-averaged relative humidity between 500 and 200 hPa. We will refer to these three MMF "actual" quantities with no abbreviations to avoid confusion.

2.2. Observation

Two observational datasets are used: geo-stationary satellite infrared radiances [*Tian et al.*, 2004] and TRMM precipitation radar reflectivities [*Liu and Zipser*, 2008; *Liu et al.*, 2008].

IR radiances are denoted by equivalent black body brightness temperatures (T_b) in water vapor (6.7 μm, $T_{6.7}$) and window (11 μm, T_{11}) channels. The 3-hourly T_b data are used at a pixel resolution of 0.1^o longitude-latitude between 30^oN and 30^oS. Based on T_{11} and $T_{6.7}$, we retrieve a precipitation index (PI), high-level cloud amount (CLD) and clear-sky upper tropospheric relative humidity (UTH) at each pixel. The retrieval algorithm is summarized in Table 1 and interested readers may refer to *Tian et al.* [2004] and *Soden and Bretherton* [1993, 1996] for details.

The precipitation radar on the TRMM satellite [*Kummerow et al.*, 1998] measures reflectivity with a horizontal resolution of 4.3 km by 4.3 km at nadir and a vertical resolution

of 250 meters from the surface to 20 km. At the frequency of 13.8 GHz, the measured reflectivity is primarily sensitive to precipitation hydrometeors. In this study, the University of Utah TRMM database [*Nesbitt et al.*, 2000; *Liu et al.*, 2008] provides the occurrence climatology of 20 dBZ or greater reflectivity at different altitudes. A reflectivity in excess of 20 dBZ signifies precipitation has been detected [*Liu et al.*, 2007]. The 20 dBZ or greater occurrence climatology is obtained by accumulating TRMM PR pixels with reflectivity $\geqslant$ 20 dBZ from 2 km to 15 km at 1 km intervals separately for land and ocean between 20^oS and 20^oN in July and January during the 9 years 1998 to 2006. Data from altitudes below 2 km are ignored because of ground clutter.

2.3. The IR T_b and PR simulators

The IR T_b simulator is a generalized forward radiative transfer model for HIRS-14 [*Soden et al.*, 2000; *Tian et al.*, 2004], which calculates clear-sky and all-sky T_{11} and $T_{6.7}$ from the MMF CRM vertical profiles of temperature, water vapor and cloud condensates. To obtain the cloud emissivity, the ice absorption coefficient is calculated according to *Ebert and Curry* [1992] assuming that the ice particle effective radius is an increasing function of temperature and 140 m^2/kg is used for the liquid absorption coefficient.

We treat every 4 km MMF CRM grid column as if it were a satellite pixel, and apply the retrieval algorithm in Table 1 to each CRM grid column in each GCM grid box. To compare the IR T_b simulator results with geo-stationary satellite data, the PI, CLD and UTH at the MMF CRM grid columns are averaged to the GCM grid box in the resolution of 2.5^o longitude and 2.0^o latitude between 30^oS and 30^oN and data from geo-satellite pixels are likewise averaged.

Some studies have remarked that the IR T_b threshold technique in the retrieval algorithm does not provide any information from inside clouds as it is only sensitive to cloud top temperatures, which might be similar for deep convective and thick cirrus clouds [*Liu et al.*, 1995; *Hall and Vonder Haar*, 1999; *Hong et al.*, 2006]. Model evaluations may also suffer from such T_b similarity particularly if there is an over abundance of high-level clouds [*Slingo*, 2004]. Because the PR simulator can overcome this potential deficiency, it is a useful complement to the IR simulator.

The PR simulator is QuickBeam [*Haynes et al.*, 2007] (http://cloudsat.atmos.colostate.edu/radarsim) version 1.03d with modifications by Roger Marchand to increase computational speed [*Marchand et al.*, 2008]. The inputs are the MMF CRM vertical profiles of temperature, relative humidity and its five hydrometeor species which are cloud ice, cloud water, rain, snow and graupel. The outputs are the vertical profiles of attenuation-corrected volume reflectivity (dBZ) at the frequency of the TRMM radar. QuickBeam allows users to specify different hydrometeor classes based on five types of size distributions: modified gamma, exponential, power law, monodisperse, and lognormal. The assumptions we use are, for cloud water, a lognormal distribution, for cloud ice, a modified gamma distribution [*Mitchell et al.*, 1996], and for rain, snow and graupel, an exponential distribution according to *Marshall and Palmer* [1948] in which fixed intercept parameters are used [*Khairoutdinov and Randall*, 2003]. The assumptions on precipitation are the same as those used in the microphysics of the embedded CRM [*Khairoutdinov and Randall*, 2003].

Figure 1 illustrates the application of both simulators to a snapshot of one of the CRMs embedded in the MMF. In the top panel, dots indicate the level where the temperature

equals that of the simulated T_b. One can clearly see a close association between this level and the highest level of significant cloud ice or water. In the lower panel, the blue contour lines show the reflectivity from the PR simulator, which has a good association with significant amounts of rain, snow and graupel.

3. The MMF vs. Geo-stationary Satellite Data

3.1. Map of daily means and diurnal cycles

Figure 2 shows July daily means and diurnal cycles of surface precipitation rate from TRMM (top panel) and MMF (second panel) as well as PI from geo-satellite data (third panel) and the IR T_b simulator applied on the MMF (bottom panel). Because of the sampling issue, the diurnal cycle of TRMM precipitation at the resolution of 2.5^o longitude by 2.0^o latitude is not shown. The diurnal cycle is constructed from 3-hourly data and is decomposed using a Fourier transform [*Tian et al.*, 2004]. Based on the first harmonic, the diurnal amplitude is the half of the difference between maximum and minimum and the diurnal phase arrow points to the local standard time (LST) of the maximum.

As PI has been viewed as an indication of precipitation from deep convection in numerous studies [*Richards and Arkin*, 1981; *Hendon and Woodberry*, 1993; *Soden et al.*, 2000; *Yang and Slingo*, 2001; *Tian et al.*, 2004], we expect a good relationship between PI and the actual surface precipitation rate. The MMF actual precipitation rate displays magnitudes and geographical distributions in the daily means that are comparable to those in both the TRMM PR observed precipitation rate and the geo-satellite PI. In contrast, the tropical and daily mean simulator PI of 13.4 mm/day is in excess of the satellite PI of 2.9 mm/day or the MMF actual precipitation rate of 3.3 mm/day. This difference is especially prominent in the region from east Africa to the west Pacific, where an overestimate

of the diurnal amplitude is also found with diurnal maxima in the morning. Moreover, the simulator PI is inconsistent with the satellite PI in the diurnal phase over land regions, such as Africa.

3.2. Land-sea diurnal composites

Figure 3 shows the diurnal anomaly composites for tropical ocean (left) and land (right) of geo-satellite data (top), simulator results (middle) and the MMF actual quantities (bottom) in July. Table 2 shows details of the diurnal amplitudes (in bold), daily means (in plain) and normalized amplitudes (in brackets) which are computed by dividing the former by the latter.

In Figure 3, geo-satellite data display a diurnal phase relationship: over ocean (land), PI peaks at 0600 (1800) LST, follows the CLD maximum at 1500 (2100) LST and the UTH maximum around midnight (0300 LST). The phase lag between PI, CLD, and UTH is about 6-9 hours over ocean and 3-6 hours over land. This suggests a simple picture in which deep convection (inferred from PI) leads to high-level anvil cloud generation and the anvil cloud dissipation results in moisturizing the upper troposphere [*Tian et al.*, 2004]. Furthermore in Table 2, the geo-satellite data exhibit greater values over land than over ocean with normalized diurnal amplitudes over land triple the corresponding value over ocean for both PI and CLD and double the ocean value for UTH.

There are three major inconsistencies between simulator results and the geo-satellite data shown in Figure 3. First the simulator PI over land peaks at 0600 LST and is out of phase with the satellite data. Second the simulator CLD over ocean has a diurnal maximum at 0600 LST and is out of phase with the satellite observation. Thirdly the diurnal amplitude of the simulator PI over ocean is largely overestimated and is even

larger than the one of the simulator PI over land, which is contradictory to the satellite data. Due to the first two, the diurnal-phase-lag relationship in the observed PI, CLD and UTH is not represented in the simulator results. Furthermore in Table 2, the daily means of simulator PI are largely overestimated as shown in Figure 2. In addition, the daily means of simulator CLD almost double the satellite data while the diurnal amplitudes are underestimated over both land and ocean .

Because geo-satellite infrared PI might be biased in representing the actual surface precipitation [*Liu et al.*, 2007], diurnal composites of TRMM PR observed precipitation rate over land and ocean are also shown in Figure 3 and Table 2. In contrast to the simulator results, the diurnal phase of the MMF actual precipitation rate agrees well with both geo-satellite data and TRMM data over land and ocean, consistent with *Khairoutdinov et al.* [2005]; the diurnal amplitude is weak over land, however this improves in January (section 6.1). The daily mean precipitation rate is overestimated especially over ocean. The MMF actual high-level cloud behaves in a very similar way as the simulator CLD with diurnal phase errors, underestimates in the diurnal amplitudes and overestimates in the daily means.

Both the simulator UTH and the MMF actual upper troposphere humidity have reasonable daily means and diurnal phase variation, although the diurnal amplitudes are not as large as the satellite data. Figure 4 shows the diurnal probability anomaly histogram for UTH from satellite data (top row) and the simulator results (bottom row). UTH data are distributed among 5% bins at each 3-hour period. Probabilities are calculated in each bin at each 3-hourly period by dividing the number of data in that bin by the total number of data among all the bins at that time period. Finally diurnal probability anomalies in

each bin at each 3-hourly period are acquired by removing the daily mean of that bin to emphasize the diurnal variation. Thus positive (negative) contour suggests at which local times, certain temperature values prefer (dislike) to occur. Observations over both ocean and land show that high clear-sky UTH (>70%) maximizes during midnight and minimizes at noon, while low UTH (<70%) tends to behave in the opposite way [*Tian et al.*, 2004]. The simulator UTH agrees with the observation quite well although the MMF underestimates the diurnal amplitude over land and there is a 2-3 hour phase lead relative to observations in high UTH.

3.3. T_b

The overestimation in the simulator PI, CLD and the MMF actual high-level cloud amount suggests an excessive amount of radiatively significant high-level cloud in MMF. Furthermore the diurnal phase error over tropical land in the simulator PI while not in the MMF actual surface precipitation rate suggests an inconsistency with the observations in the simulated relationship between high-level clouds and precipitation. In order to investigate these biases in a more simple manner, we examine the IR simulator T_{11} and $T_{6.7}$, based on which the PI, CLD and UTH are retrieved.

Figure 5 shows the probability density function (left) and cumulative probability (right) of T_{11} over tropical land regions. Although not shown, similar behavior of T_{11} and $T_{6.7}$ is also found over tropical oceans and in the comparison of less aggregated data, *e.g.* between the CRM grid and the satellite pixel data.

Clearly, below 260 K, a cold bias is found in the simulator T_{11} (solid) as compared to satellite data (dashed). The deep convective clouds (DCC, or hot tower, with $T_{11} < 230$ K), is about 9% from the simulator and only 3% from the satellite data. Since

PI is proportional to the difference between 230 K and T_{11} (Table 1), the colder T_{11} leads to larger PI, thus explaining the bias of the daily mean PI. The CLD ($T_{11} < 260$ K), is about 21% in the simulator compared to 14% in the satellite data. Clear-sky UTH is retrieved when $T_{11} > 260$ K, where the discrepancy becomes smaller between observation and simulator results, which explains why UTH behaves better.

If the cold bias in T_{11} explains the overestimation of the daily mean simulator PI and CLD, then how is the diurnal phase error related? Figure 6 shows the histograms of the diurnal probability anomalies of T_{11}, which is calculated in the same way as in Figure 4 but among 5 K T_{11} bins at each 3-hour period.

In Figure 6, the satellite data (reproduced from *Tian et al.* [2004]) show that over ocean, the DCC ($T_{11} < 230$ K) peaks in the morning while convective anvil cloud (CAC, $230 \text{ K} < T_{11} < 260$ K) peaks in the late afternoon, whereas over land, the CAC maximum tends to occur after the DCC maximum with a few hours' lag in the evening. Satellite T_{11} over ocean has a smaller diurnal variation than over land. The most prominent difference shown in simulator results is the diurnal evolution of T_{11} colder and warmer than 220 K. When warmer than 220 K, the simulator T_{11} changes in a manner similar to the observation, however with a larger variation over ocean than over land. When colder than 220 K, the simulator T_{11} peaks in the morning and minimizes in the afternoon over both ocean and land. The behavior of T_{11} beneath and above 220 K are out of phase with each other, but with a much larger diurnal variation when T_{11} is colder than 220 K. This explains the diurnal phase error in the simulator PI and CLD in Figure 3.

3.4. High-level clouds

Why the T_{11} diurnal cycle flips sign when crossing the 220 K threshold? We believe this is because clouds at different levels have different diurnal cycles. Figure 7 shows the diurnal anomalies of GCM-grid-box-mean cloud ice. The anomaly is attained by removing the daily mean value at each level. At levels above 250 hPa, the diurnal anomaly of cloud ice peaks in the early morning over both ocean and land; while below 250 hPa, it peaks in the late afternoon over ocean and during midnight over land. Such behavior is very similar to T_{11} above and beneath 220 K. Because the 250 hPa temperature is around the threshold temperature for PI of 230 K, this suggests that it is the diurnal cycle of cloud ice above 250 hPa which is responsible for the erroneous diurnal cycle in PI.

Given the cold bias in T_{11} as well as the fact that over land the simulator PI is out of phase with MMF actual surface precipitation, we must ask if we are detecting true deep convective hot tower clouds in MMF by selecting CRM columns with $T_{11} < 230$ K. To answer this we examined snapshots like those in Figure 1. The extreme cold T_{11} often coincides with an overcast cloud layer between 400 hPa and 150 hPa, or even higher, and usually persists for several days before dissipation. We also find such high-level cloud layer sometimes with deep convective cloud tower attached to it and sometimes not. Since the MMF output data is 3-hourly, it is really hardly to say whether these high-level clouds are anvil clouds associated with deep convection or not. However it is clear that a significant portion of high-level clouds with IR $T_{11} < 230$ K are not true deep convection hot tower clouds, but these thick long-lasting high-level clouds.

The excessive high-level cloud has long existed in the standard CAM3 (or older version) simulations [*Lin and Zhang*, 2004] and improvement has been reported in MMF [*Khairout-*

dinov et al., 2005]. However *Khairoutdinov et al.* [2005] estimated high-level cloud fraction approximately based on the ice water path above 400 hPa, whereas we make a more accurate comparison based upon applying the satellite retrieval algorithm to simulator T_b. Thus we feel confident in our conclusion that MMF overestimates the amount of high-level cloud. This conclusion has also been found in other MMF evaluation studies including *McFarlane et al.* [2007], who pointed out that the MMF largely overestimates the deep convection and thick cirrus cloud occurrence frequency at the tropical western Pacific ARM sites. Using CloudSat cloud radar data, *Marchand et al.* [2008] also found that MMF has excessive hydrometeor coverage in several deep convection regions at all altitudes.

4. The MMF vs. TRMM data

Below we present results for PR reflectivities $\geqslant$ 20 dBZ, which is considered as evidence of strong convective updrafts that lift more and/or larger ice particles to higher altitudes [*Liu et al.*, 2007].

Figure 8 shows the PR 20 dBZ or greater occurrence fraction in July in tropics (20^oS-20^oN) as a function of altitude above sea level. The occurrence fraction is obtained by dividing the number of TRMM pixels (data at CRM column height levels) with reflectivity $\geqslant$ 20 dBZ at a given altitude by the total number of TRMM samples (CRM columns). The occurrence fraction at a certain altitude suggests the potential for deep convective updrafts to reach that altitude. Both the TRMM data and the PR simulator results clearly show that there are less strong updrafts at higher altitudes. For instance, the TRMM data suggests that the potential to observe a deep convective case over land is about 1% at 6 km, 0.1% at 10 km and 0.01% at 14 km.

Although there is good agreement over land, over ocean the 20 dBZ or greater occurrence fraction from the PR simulator is almost one order of magnitude larger than the TRMM data, at altitudes above 6 km. This suggests the MMF oceanic deep convection is too frequent resulting in too many strong updrafts that penetrate to high altitudes. TRMM data suggest that deep convection tends to be more active over land than over ocean above 6 km. Such land-sea contrast is not captured in PR simulator results, implying that there is little land-sea distinction in the incidence of MMF deep convection. However if we pay attention to extreme intense deep convections represented by PR reflectivities $\geqslant$ 40 dBZ, the occurrence fraction is greater over land than ocean in the MMF above 4 km.

Figure 9 displays the composite diurnal cycle of the 20 dBZ or greater occurrence fraction in tropics at 6 km, 10 km and 14 km. The TRMM data shows a much more pronounced diurnal variation over land than ocean at all the three levels, however, the PR simulator results behave the opposite way. Over ocean (land), the TRMM data always has a minimum (maximum) at 1800 LST, and maximum (minimum) in the morning. While the simulator results generally indicate similar phase to the maxima and minima, the amplitude of the diurnal variation is far too small over land at all the three levels and too large over ocean at 10 and 14 km. Furthermore at 14 km, the occurrence fraction over land has a secondary peak at 0600 LST which is inconsistent with the TRMM data; this might be related to the phase error found in PI and CLD from the IR T_b simulator shown in Figure 3. Note that the diurnal cycle of the 20 dBZ or greater occurrence fraction improves somewhat in January especially over land (section 6.1).

5. Results from the joint distribution of MMF simulated IR T_b and PR Reflectivity

What can we learn about MMF deep convection by using both simulators simultaneously? Here, we investigate the statistics of CRM columns with both IR $T_{11} < 230$ K and PR reflectivity $\geqslant$ 20dBZ anywhere in the vertical column, which may be a better indicator of deep convective clouds than either measure individually.

The color shading in Figure 10 depicts at each GCM grid box in the MMF, the probability (in percent) to detect a deep convective CRM column using different measures: both simulators (top); the IR T_b simulator only (middle); and the PR simulator only (bottom). More than 50% of the CRM columns are observed to have $T_{11} < 230$ K in regions from the Indian Ocean to the Northwest Pacific, and more than 30% in East cenral Africa and the Arabian Peninsula. However the top panel demonstrates that in these regions, fewer than 30% of the CRM columns with $T_{11} < 230$ K have radar reflectivity $\geqslant$ 20dBZ. Although some deep convection clouds may not produce precipitation if they are still in the initial stage of development, this probably can not explain this large difference. Rather this suggests that a large portion of clouds with $T_{11} < 230$ K in the MMF are not deep convective clouds (DCCs), which further confirms our finding in section 3. On the other hand, comparison between the top and bottom panels of Figure 10 reminds us that some convective CRM columns detected by the PR simulator with reflectivity $\geqslant$ 20dBZ may not penetrate deep enough to have the cloud top $T_{11} < 230$ K; this is particularly true over central Africa and Amazon.

If we define deep convective hot tower clouds as those CRM columns which jointly have IR $T_{11} < 230$ K and PR reflectivity $\geqslant$ 20 dBZ, can we detect land-ocean difference in the

intensity of convection in MMF? Figure 11 shows the cumulative probability of in-cloud melting-level updrafts of these CRM columns. Melting level is determined by the vertical profile of temperature at each of the CRM columns. Each data point represents the probability of the updraft above certain limit, e.g., only about 10% of these columns have updrafts greater than 1.5 m/s. Note that we are examining only the 50% of these columns for which the instantaneous vertical velocity is upward at the melting level. Although our use of 3-hourly snapshot data may hinder a definitive assessment, Figure 11 may suggest that in MMF the convective updrafts are weak, compared to median values of several m/s indicated by observations [*Zipser et al.*, 2006; *Liu et al.*, 2007], independent CRM [*Xu and Randall*, 2001; *Li et al.*, 2008] and GCM updraft studies [*Del Genio et al.*, 2007]. However in the tail of the updraft distribution, we do find more deep convective hot towers with stronger updrafts over land relative to ocean. For example, about 0.3% of the MMF hot towers have updrafts in excess of 8.5 m/s over land whereas only 0.1% of the hot towers over ocean have updrafts in excess of this value.

Figure 12 shows the probability for PR reflectivity of 20 dBZ or greater to be found at a given height in each 1 m/s bin of the deep-convective in-cloud melting-level updrafts. The probability is obtained by dividing the number of CRM columns with 20 dBZ or greater at a given height in a given updraft bin by the total number of CRM columns in the same bin. Although there is sampling noise at large values of updraft strength, it is clear that with increasing updraft strength, precipitation particles penetrate to a higher altitude, which is consistent with the assumption that radar reflectivity is proportional to convective intensity. Moreover, at same updraft strength, precipitation particles reach a

greater depth over land than over ocean. This suggests that the MMF is able to represent some aspects of the observed land-sea contrast [*Zipser et al.*, 2006; *Liu et al.*, 2007].

If we recompute the precipitation index (in Figure 2 and 3) from those CRM columns that have both IR $T_{11} < 230$ K and PR reflectivity $\geqslant 20$ dBZ, we still find a diurnal phase bias over land although the daily mean overestimation (Table 2) is largely mitigated. Assuming that we are detecting hot towers by use of the two simulators together, this suggests a phase error in which there are too many hot towers over land in the morning relative to the late afternoon.

6. Discussion

6.1. MMF boreal winter

Khairoutdinov et al. [2005] reported well-simulated surface precipitation in MMF boreal winter and excessive boreal summer precipitation in the Western Pacific due to overactive Southeast Asian Monsoon. *Luo and Stephens* [2006] attributed the summer precipitation bias to an enhanced convection-evaporation-wind feedback during monsoon season. The analysis above focuses on the month of July. Then do we reach the same conclusions with data in January?

Figure 13, 14, 15, 16 and Table 3 show the same comparisons between observation, simulator results and the MMF actual quantities as in Figure 2, 3, 8, 9 and Table 2 respectively but for January. Comparing Figure 13 with 2, seasonal variation in the daily mean precipitation rate is shown with more precipitation over tropical land regions in January. MMF actual surface precipitation rate agrees well with TRMM and Geo-stationary satellite PI data in the daily mean field while the simulator PI is still largely overestimated especially in the region from east Africa to west Pacific. Comparing Figure 14

with 3, there is notable improvement in the diurnal cycle amplitude of the MMF actual surface precipitation rate over land in January and the normalized diurnal amplitude is also improved comparing Table 3 and 2. However the daily mean MMF actual surface precipitation rate over ocean is still overestimated and the diurnal-phase-lag relationship between observed PI, CLD and UTH is still not represented in both the simulator results and the MMF actual quantities. Compared with Figure 8, the only difference in Figure 15 is the overestimation in MMF 20 dBZ or greater occurrence fraction at levels around 10 km over land. Furthermore Figure 16 shows the MMF 20 dBZ or greater occurrence fraction tends to have a larger diurnal amplitude over land than over ocean at all the three levels which is not evident in Figure 9. However compared with TRMM data in January, the MMF oceanic deep convection is still overactive. Furthermore, there is still little land-sea contrast in the MMF 20 dBZ or above occurrence fraction; the land-sea contrast only becomes apparent for extremely intense events with reflectivity above 40 dBZ. Thus the investigation on January MMF data leads to very similar conclusion as on July MMF data and the model biases we find are independent of the excessive summer precipitation bias in MMF.

6.2. Uncertainties in the simulators

In the computation of infrared T_b, the radiative properties of cloud ice and water are specified from *Ebert and Curry* [1992] and are identical to those used in the CAM. The most sensitive parameter is the ice mass absorption coefficient, k_i. If we reduce k_i to 1/3 of its original value, the cold bias shown in Figure 5 decreases and the simulated $T_{6.7}$ and T_{11} are comparable to the observed values. However, such reduction lowers the value of k_i outside of its uncertainty range (Q. Fu and X. Huang, personal communications). Even

with this reduction, the phase bias of PI and CLD shown in Figure 3 remains, which is understandable given the diurnal cycle of cloud ice (Figure 7).

Radar reflectivities are sensitive to the assumed size distribution of the precipitation hydrometeors in simulators [*Blossey et al.*, 2007]. We use those of *Marshall and Palmer* [1948], which are identical to those assumed by the embedded CRM in its calculation of bulk microphysical process rates. Although the simulation would be different, we treated the graupel in the radar simulator as if it were snow, effectively reducing the equivalent volume sphere size of the graupel particles. This reduces the 20 dBZ or greater occurrence fraction, particularly between 6 km and 10 km in Figure 8. These altitudes are just above the freezing level in the tropics where the temperature dependent partitioning of hydrometeor assumes graupel occurs. However, this change removes only about 15% of the oceanic overestimation by MMF shown in Figure 8 and 9.

6.3. Why biased?

Given that the conclusion that MMF has an excessive amount of high-level clouds and precipitation hydrometeors particularly over ocean is robust to uncertainties in the comparison of model to observations, the next question is what are the causes of this bias? Below we present some possible causes of this bias, but we do not judge which are responsible as this requires a large number of experiments which is not feasible given MMF's heavy computational expense.

The overestimate in high-level clouds may result from biases in the cloud formation and dissipation. To form clouds, moisture supply is a must, which must come from vertical transports. From the PR simulator, MMF deep convection over ocean is too frequent by almost one magnitude in 20 dBZ or greater occurrence fraction, especially at the

altitudes above 6 km. One possible interpretation of this result is that with overactive oceanic deep convection, MMF overestimates the moisture transported from lower to upper troposphere, favoring the high-level cloud generation. One potential explanation for the overactive oceanic deep convection is the enhanced convection-evaporation-wind feedback identified by *Luo and Stephens* [2006] during Asian summer monsoon season. According to their study, this enhanced feedback is linked to the cyclic boundary condition of the embedded CRM as the clouds and moisture reenter the CRM domain rather than advecting away. Additionally, impacts with a 3-dimensional CRM in the MMF instead of the default 2-dimensional CRM have demonstrated significant influence on tropical precipitation and water vapor [*Khairoutdinov et al.*, 2005; *Luo and Stephens*, 2006].

The MMF CRM uses a simple bulk microphysics parameterization [*Khairoutdinov and Randall*, 2003], in which the partitioning between hydrometeors is solely temperature dependent. The dissipation of high-level clouds is affected by the terminal velocities of hydrometeors and the parameterized rates of ice autoconversion and aggregation. Changes in these parameterizations will certainly lead to changes in cloud condensate and precipitation and may significantly affect the high-level cloud amount. Furthermore, observations indicate that the particle size distributions on land and ocean are very different [*Rosenfeld and Lensky*, 1998], however there is no distinct treatment in the model. This may affect the PR 20 dBZ statistics since the radar signal is very sensitive to the particle size.

The extensiveness of high-level clouds could be attributed to the lack of strong penetrating updrafts. Specifically, if there are not enough convective updraft overshoots at the top of deep convective clouds, the compensating subsidence will be weak and unable to limit the expansion of convective anvil clouds. Figure 11 suggests that the convective

updrafts in MMF appear weak compared with observations [*Zipser et al.*, 2006; *Liu et al.*, 2007], independent CRM [*Xu and Randall*, 2001; *Li et al.*, 2008] and GCM updraft studies [*Del Genio et al.*, 2007]. This is presumably related to the coarse resolution of the MMF CRM in both the horizontal and vertical dimensions. *Khairoutdinov and Randall* [2003] showed that the variance of vertical velocity in SAM increases with finer horizontal resolution. In a CRM radiative-convective equilibrium study, *Pauluis and Garner* [2006] showed that a coarser horizontal resolution may lead to flat parcels rising with a slower pace; however, they also suggested that deep convective cloud ice and convective outflow are not very sensitive to resolutions less than 16 km.

7. Summary

In this study we evaluate the diurnal cycle of precipitation, high-level cloud, upper tropospheric water vapor by applying the IR T_b and PR simulators to the MMF CRM grid scale data. The precipitation index (PI), high-level cloud amount (CLD) and upper tropospheric relative humidity (UTH) from the IR T_b simulator are compared to geostationary satellite data and the occurrence of the reflectivity greater than 20 dBZ from the PR simulator is compared to the TRMM data. Combining both simulators, the properties of convective updrafts are investigated.

From the IR T_b simulator study, excessive high-level cloud is found in MMF with cloud ice maxima in the early morning at levels above 250 hPa over both ocean and land. This leads to the cold bias and diurnal phase errors in T_{11}. Such bias further results in the failure of MMF to represent the diurnal-phase-lag relationship among PI, CLD and the clear-sky UTH from the geo-satellite observation [*Tian et al.*, 2004]. Specifically,

the simulator PI over land and the simulator CLD over ocean are out of phase with the satellite data. The daily mean of the simulator PI and CLD are greatly overestimated.

Compared with both geo-satellite PI and TRMM PR observed precipitation rate, the MMF actual precipitation rate has a reasonable diurnal variation especially in January. However, a weak diurnal amplitude is identified over land in July and the oceanic daily mean precipitation is overestimated. The MMF actual high-level cloud behaves very similarly as the simulator CLD. The MMF clear-sky UTH tends to agree well with observations in both daily mean and the diurnal variation.

Based on the occurrence of 20 dBZ or greater reflectivity from the PR simulator, the MMF oceanic deep convection occurs much more frequently than the TRMM observation. Moreover, MMF exhibits little distinction between tropical land and ocean in the occurrence fraction of reflectivity $\geqslant$ 20 dBZ, contrary to TRMM. However, extremely intense convection with reflectivity $\geqslant$ 40 dBZ is found more often over land than ocean. In examination of the diurnal cycle, MMF overestimates the occurrence of reflectivity $\geqslant$ 20 dBZ during the whole diurnal cycle at levels of 6, 10 and 14 km over ocean. Over land, the MMF diurnal cycle tends to behave better in January than in July although MMF underestimates the diurnal maximum at levels of 6 and 14 km.

From the CRM columns in which PR reflectivity $\geqslant$ 20 dBZ and IR $T_{11} < 230$ K cooccur, we examine the properties of deep convective towers. The analysis shows that stronger updrafts penetrate deeper and that extremely intense updrafts are found more often over land than over ocean.

In spite of these problems in the simulation of the diurnal cycle, MMF is still superior to conventional GCMs in many aspects. The diurnal maximum of the MMF actual surface

precipitation rate occurs at sunset over land whereas GCMs tend to simulate precipitation maximums closer to noon. *Tian et al.* [2004] showed that the GFDL AM2 was not able to capture the behavior of UTH, especially in the histogram analysis (Figure 4) for which the MMF does well. Moreover the MMF captures some aspects of the land-sea contrast in that intense deep convection is found more often over land than over ocean and usually penetrates deeper. Conventional GCMs may have difficulty in doing this, although one study suggests that it is feasible [*Del Genio et al.*, 2007]. From these results, we conclude that the problems in MMF are great enough to cast doubt on the ability to use MMF as a basis for improvement of the diurnal cycle of cloud and precipitation in conventional GCMs.

This study shows that it is efficient and reasonable to use simulators to compare the MMF to global observations. It would be of interest to repeat this study with other MMFs [*Tao et al.*, 2008] or a global cloud resolving model [*Miura et al.*, 2007].

Acknowledgments. The authors thank Anthony T. Hoang for assistance with data transfer and storage. The authors also express their appreciation to Jiundar Chern and Wei-Kuo Tao for valuable discussions on the MMF and to Qiang Fu and Xianglei Huang for comments on the ice absorption coefficient. This work was supported through the Department of Energy's Atmospheric Radiation Measurement which is directed from the Biological and Environmental Research program at the Office of Science. This work was performed under the auspices of the U.S. Department of Energy by Lawrence Livermore National Laboratory under Contract DE-AC52-07NA27344.

References

Arakawa, A. (1969), Parameterization of cumulus convection, in *Proc. WMO/IUGG Symp. On Numerical Weather Prediction, IV, 8, 1–6*, Japen Meteorological Angency, Tokyo, Japen.

Arakawa, A. (1975), Modeling clouds and cloud processes for use in climate model., in *The Physical Basis of Climate and Climate Modeling*, vol. 16, pp. 183–94, GARP Publications Series, ICSU/WMO.

Arakawa, A. (2004), The cumulus parameterization problems: past, present, and future, *J. Climate*, *17*, 2493–2525.

Blossey, P. N., C. S. Bretherton, and J. Cetrone (2007), Cloud-rosolving model simulations of KWAJEX: Model sensitivities and comparisons with satellite and radar observations, *J. Atmos. Sci.*, *64*, 1488–1508.

Chang, A. T. C., L. S. Chiu, and G. Yang (1995), Diurnal cycle of oceanic precipitation from SSM/I data, *Mon. Wea. Rev.*, *123*, 3371–3380.

Chen, S. S., and R. A. J. Houze (1997), Diurnal variation and lifecycle of deep convective systems over the Pacific warm pool, *Quart. J. Roy. Meteor. Soc.*, *123*, 357–388.

Collins, W. D., P. J. Rasch, B. A. Boville, J. J. Hack, J. R. McCaa, D. L. Williamson, B. P. Briegleb, C. M. Bitz, S.-J. Lin, and M. Zhang (2006), The formulation and atmospheric simulation of the community atmosphere model version 3 (CAM3), *J. Atmos. Sci.*, *19*, 2144–2161.

Dai, A. (2001), Global precipitation and thunderstorm frequencies. Part II: Diurnal variations, *J. Climate*, *14*, 1112–1128.

Dai, A., F. Giorgi, and K. Trenberth (1999), Observed and model-simulated diurnal cycles of precipitation over the contiguous United States, *J. Geophys. Res.*, *104*, 6377–6402.

Del Genio, A. D., M.-S. Yao, and J. Jonas (2007), Will moist convection be stronger in a warmer climate?, *Geophy. Res. Let.*, *34*, L16703, doi:10.1029/2007GL030525.

DeMott, C. A., D. A. Randall, and M. Khairoutdinov (2007), Convective precipitation variability as a tool for general circulation model analysis, *J. Climate*, *20*, 91–112.

Ebert, E. E., and J. A. Curry (1992), A parameterization of ice cloud optical properties for climate models, *J. Geophys. Res.*, *97(D4)*, 3831–3836, 10.1029/91JD02472.

Grabowski, W. (2001), Coupling cloud processes with the large-scale dynamics using the cloud-resolving convection parameterization (CRCP), *J. Atmos. Sci.*, *58*, 978–997.

Grabowski, W., and P. Smolarkiewicz (1999), A cloud resolving convection parameterization for modeling the tropical convective atmosphere, *Physica D*, *133*, 171–178.

Gray, W., and R. Jacobson (1977), Diurnal variation of deep cumulus convection, *Mon. Wea. Rev.*, *105*, 1171–1188.

Hall, T. J., and T. Vonder Haar (1999), The diurnal cycle of west Pacific deep convection and its relation to the spatial and temporal variations of tropical MCSs, *J. Atmos. Sci.*, *56*, 3401–3415.

Haynes, J., R. Marchand, Z. Lou, A. Bodas-Salcedo, and G.L.Stephens (2007), A multi-purpose radar simulation package: Quickbeam, *Bull. Amer. Meteorol. Soc.*, *88*, 1723–1727.

Hendon, H. H., and K. Woodberry (1993), The diurnal cycle of tropical convection, *J. Geophys. Res.*, *98*, 16,623–16,537.

Hong, G., G. heygster, and C. A. M. Rodriguez (2006), Effect of cirrus clouds on the diurnal cycle of tropical deep convective clouds, *J. Geophys. Res.*, *111*, D06209, DOI:10.1029/2005JD006208.

Houghton, J., Y. Ding, D. Griggs, M. Noguer, P. van der Linden, X. Dai, K. Maskell, and C. Johnson (2001), *Climate Change 2001: The Scientific Basis*, Cambridge University Press, 881pp.

Khairoutdinov, M. F., and D. A. Randall (2001), A cloud resolving model as a cloud parameterization in the NCAR Community Climate Model: Preliminary results, *Geophy. Res. Let.*, *28*, 3617–3620.

Khairoutdinov, M. F., and D. A. Randall (2003), Cloud resolving modeling of the ARM summer 1997 IOP: model formulation, results, uncertainties and sensitivities, *J. Atmos. Sci.*, *30*, 607–625.

Khairoutdinov, M. F., D. A. Randall, and C. DeMott (2005), Simulations of the atmospheric general circulation using a cloud-resolving model as a superparameterization of physical processes, *J. Atmos. Sci.*, *62*, 2136–2154.

Klein, S. A., and C. Jakob (1999), Validation and sensitivities of frontal clouds simulated by the ECMWF model, *Mon. Wea. Rev.*, *127*, 2514–2531.

Kraus, E. B. (1963), The diurnal precipitation change over the sea, *J. Atmos. Sci.*, *20*, 551–556.

Kummerow, C., W. Barnes, T. Kozu, J. Shiue, and J. Simpson (1998), The tropical rainfall measuring mission (TRMM), *J. Atmos. Oceanic Technol.*, *15*, 809–817.

Li, Y., E. J. Zipser, S. K. Krueger, and M. A. Zulauf (2008), Cloud-resolving modeling of deep convection during KWAJEX. Part I: Comparison to TRMM satellite and ground-

based radar observations, *Mon. Wea. Rev.*, in press.

Lin, W., and M. Zhang (2004), Evaluation of clouds and their radiative effects simulated by the NCAR Community Atmosphere Model against satellite observations, *J. Climate*, *17*, 3302–3318.

Liu, C., and E. J. Zipser (2008), Diurnal cycles of precipitation, clouds and lightning in the tropics from 9 years of TRMM observations, *Geophy. Res. Let.*, *35*, L04819, doi:10.1029/2007GL032437.

Liu, C., E. J. Zipser, and S. W. Nesbitt (2007), Global distribution of tropical deep convection: different perspectives from TRMM infrared and radar data, *J. Climate*, *20*, 489–503.

Liu, C., E. Zipser, D. Cecil, S. W. Nesbitt, and S. Sherwood (2008), A cloud and precipitation feature database from 9 years of TRMM observations, *J. Appl. Meteor. Climate.*, accepted.

Liu, G., J. A. Curry, and R.-S. Sheu (1995), Classification of clouds over the western equatorial Pacific ocean using combined infrared and microwave satellite data, *J. Geophys. Res.*, *100*, 13,811–13,826.

Luo, Z., and G. L. Stephens (2006), An enhanced convection-wind-evaporation feedback in a superparameterization GCM (SP-GCM) depiction of the asian summer monsoon, *Geophy. Res. Let.*, *33*, L06707, doi:10.1029/2005GL025060.

Marchand, R., J. Haynes, G. G. Mace, T. Ackerman, and G. Stephens (2008), A comparison of CloudSat cloud radar observations with simulated cloud radar output from the Multiscale Modeling Framework global climate model, *J. Geophys. Res.*, submitted.

Marshall, J. S., and W. M. Palmer (1948), The distribution of rain drops with size, *J. Meteor.*, *5*, 165–166.

McFarlane, S. A., J. H. Mather, and T. P. Ackerman (2007), Analysis of tropical radiative heating profiles: A comparison of models and observations, *J. Geophys. Res.*, *112*, D14218, DOI:10.1029/2006JD008290.

Mitchell, D. L., S. K. Chai, Y. Liu, A. J. Heymsfield, and Y. Dong (1996), Modeling cirrus clouds. Part I: Treatment of bimodal size spectra and case study analysis, *J. Atmos. Sci.*, *53*, 2952–2966.

Miura, H., M. Satoh, H. Tomita, T. Nasuno, S. Iga, and A. T. Noda (2007), A short-duration global cloud-resolving simulation with a realistic land and sea distribution, *Geophy. Res. Let.*, *34*, L02804,doi:10.1029/2006GL027448.

Morcrette, J.-J. (1991), Evaluation of model-generated cloudiness: Satellite-observed and model-generated diurnal variability of brightness temperature, *Mon. Wea. Rev.*, *119*, 1205–1224.

Nesbitt, S., and E. J. Zipser (2003), The diurnal cycle of rainfall and convective intensity according to three years of TRMM measurements, *J. Climate*, *16*, 1456–1475.

Nesbitt, S., E. J. Zipser, and D. J. Cecil (2000), A census of precipitation features in the tropics using TRMM: Radar, ice scattering, and lightning observations, *J. Climate*, *13*, 4087–4106.

Ovtchinnikov, M., T. Ackerman, R. Marchand, and M. Khairoutdinov (2006), Evaluation of the Multiscale Modeling Framework using data from the Atmospheric Radiation Measurement program, *J. Climate*, *19*, 1716–1729.

Pauluis, O., and S. Garner (2006), Sensitivity of radiative-convective equilibrium simulations to horizontal resolution, *J. Atmos. Sci.*, *63*, 1910–1923.

Randall, D. A., Harshvardhan, and D. A. Dazlich (1991), Diurnal variability of the hygrologic cycle in a general circulation model, *J. Atmos. Sci.*, *48*, 40–62.

Randall, D. A., M. F. Khairoutdinov, A. Arakawa, and W. W. Grabowski (2003), Breaking the cloud-parameterization deadlock, *Bull. Amer. Meteorol. Soc.*, *84*, 1547–1564.

Richards, F., and P. A. Arkin (1981), On the relationship between satellite observed cloud cover and precipitation, *Mon. Wea. Rev.*, *109*, 1081–1093.

Rosenfeld, D., and I. M. Lensky (1998), Satellite-based insights into precipitation formation processes in continental and maritime convective clouds, *Bull. Amer. Meteor. Soc.*, *79*, 2457–2476.

Short, D. A., and J. M. Wallace (1980), Satellite-inferred morning-to-evening cloudiness changes, *Mon. Wea. Rev.*, *108*, 1160–1169.

Short, D. A., P. A. Kucera, B. S. Ferrier, J. C. Gerlach, S. A. Rutledge, and O. W. Thiele (1997), Shipboard radar rainfall patterns within the TOGA COARE IFA, *Bull. Amer. Meteorol. Soc.*, *115*, 2817–2836.

Slingo, A. (2004), Simulation of the diurnal cycle in a climate model and its evaluation using data from Meteosat 7, *Quart. J. Roy. Meteor. Soc.*, *130*, 1449–1467.

Soden, B. J., and F. P. Bretherton (1993), Upper tropospheric relative humidity form the GOES 6.7 μm channel: Method and climatology for July 1987, *J. Geophys. Res.*, *98*, 16,669–16,688.

Soden, B. J., and F. P. Bretherton (1996), Interpretation of TOVS water vapor radiance in terms of layer average relative humidities: Method and climatology for the upper,

middle and lower troposphere, *J. Geophys. Res.*, *101*, 9333–9343.

Soden, B. J., S. Tjemkes, J. Schmetz, R. Saunders, J. Bates, B. Ellingson, R. Engelen, L. Garand, D. Jackson, G. Jedlovec, T. Kleespies, D. Randel, P. Rayer, E. Salathe, D. Schwarzkopf, N. Scott, B. Sohn, S. de Souza-Machado, L. Strow, D. Tobin, D. Turner, P. van Delst, and T. Wehr (2000), An intercomparison of radiation codes for retrieving upper-tropospheric humidity in the 6.3-μm band: A report from the first GVaP workshop, *Bull. Amer. Meteorol. Soc.*, *81*, 797–808.

Sui, C.-H., K.-M. Lau, Y. N. Takayabu, and D. A. Short (1997), Diurnal variation in tropical oceanic cumulus convection during TOGA COARE, *J. Atmos. Sci.*, *54*, 639–655.

Tao, W.-K., J. Chern, R. Atlas, D. Randall, X. Lin, M. Khairoutdinov, J.-L. Li, D. E. Waliser, A. Hou, C. Peters-Lidard, W. Lau, and J. Simpson (2008), A Multi-scale Modeling System: Developments, applications and critical issues, *Bull. Amer. Meteorol. Soc.*, accepted.

Tian, B., B. J. Soden, and X. Wu (2004), Diurnal cycle of convection, clouds, and water vapor in the tropical upper troposphere: Satellites versus a general circulation model, *J. Geophys. Res.*, *109*, D10101, DOI:10.1029/2003JD004117.

Wyant, M. C., M. Khairoutdinov, and C. S. Bretherton (2006), Climate sensitivity and cloud response of a GCM with a superparameterization, *Geophy. Res. Let.*, *33*, L06714, DOI:10.1029/2005GL025464.

Xu, K.-M., and D. Randall (2001), Updraft and downdraft statistics of simulated tropical and midlatitude cumulus convection, *J. Atmos. Sci.*, *58*, 1630–1649.

Yang, G.-Y., and J. M. Slingo (2001), The diurnal cycle in the tropics, *Mon. Wea. Rev.*, *129*, 784–801.

Zipser, E. J., D. J. Cecil, C. Liu, S. W. Nesbitt, and D. P. Yorty (2006), Where are the most intense thunderstorms on earth?, *Bull. Amer. Meteorol. Soc.*, *87*, 1057–1071.

	$T_{11} > 260$ K	230 K $< T_{11} <$ 260 K	$T_{11} < 230$ K
PI	0	0	a_p(230-T_{11})
CLD	0	1	1
UTH	(cosθ/p_0)exp(a+b$T_{6.7}$)	-999.	-999.

Table 1. Retrieval algorithm at each pixel (each CRM grid column) in each satellite (GCM) grid box of the resolution 2.5^o longitude by 2.0^o latitude. $a_p = 6.96$ mm day^{-1} K^{-1}. θ is the satellite zenith angle; p_0 term denotes the dependence of $T_{6.7}$ on air temperature; a = 27.9, and b = -0.10. "-999." is a missing value flag which is assumed for clear-sky UTH when cloudy.

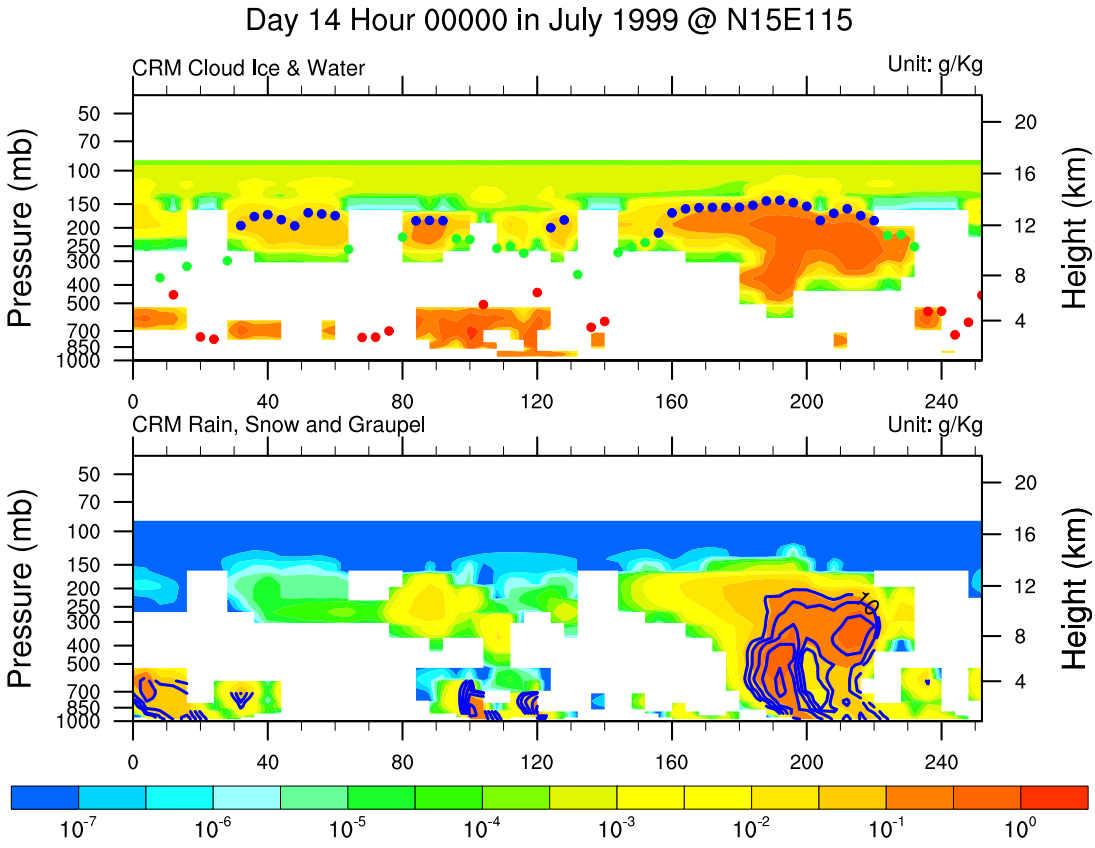

Figure 1. The snapshot of the MMF CRM clouds and precipitation at 0 UTC on July 14th, 1999 at 15^{o}N,115^{o}E. The y-axis is the pressure (height) levels. The x-axis is the CRM grid distance (km) with a 4 km spacing along the west-east direction. The color shading shows the sum of the mixing ratio (g/kg) in the logarithm scale (log10): for cloud ice and cloud water in the top panel; for rain, snow and graupel in the bottom panel . In the top panel, the dots show the equivalent T_{11} heights, retrieved from the infrared T_b simulator, according to the CRM vertical air temperature profiles. Blue dots denote $T_{11} < 230$k; green dots denote $230\text{k} < T_{11} < 260$k; red dots denote $T_{11} > 260$k. In the bottom panel, the blue line contours show the radar reflectivity from the precipitation radar simulator, starting from 10 dBZ with an interval of 5 dBZ.

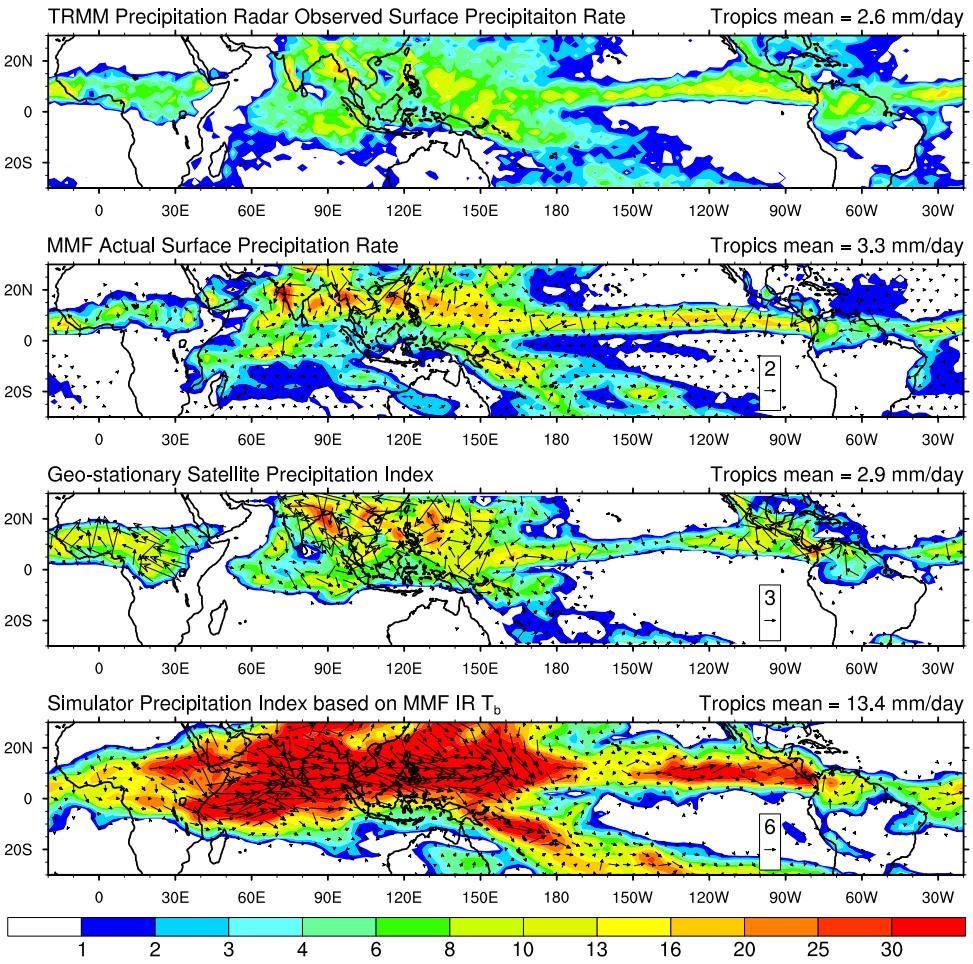

Figure 2. Maps of daily means and the monthly mean diurnal cycles: surface precipitation rate from TRMM precipitation radar in July averaged over years 1998 to 2006 (top); the MMF actual surface precipitation rate in July 1999 (second); precipitation index (PI) from geo-stationary satellite in July 1999 (third); PI from the IR T_b simulator applied to the MMF in July 1999 (bottom). Color shading shows daily means in mm/day. Tropical (30^oS to 30^oN) mean values are shown at the up-right corner of each panel. The length of the vector denotes the diurnal amplitude (mm/day). Notice the different scales of the vector length in the legend of each panel. Diurnal phase is represented by a 24-hour clock: upward arrow for midnight (0000 LST), rightward for dawn (0600 LST), downward for noon (1200 LST) and leftward for dusk (1800 LST).

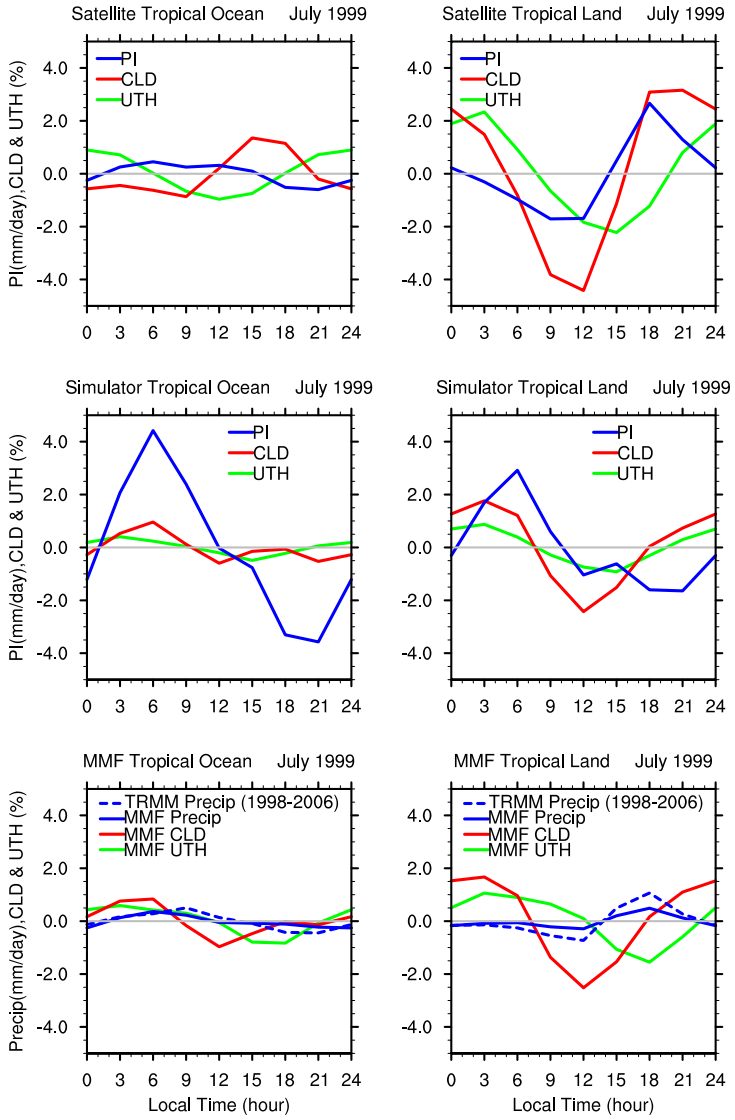

Figure 3. July 1999 diurnal anomalies of precipitation (solid blue), high-level clouds amount(CLD, in red) and upper tropospheric relative humidity (UTH, in green) for tropical land (right) and ocean (left): the precipitation index (PI), CLD and UTH based on geo-satellite observed T_b (top); PI, CLD and UTH based on T_b from the infrared T_b simulator applied to the MMF (middle); the MMF actual surface precipitation rate, high-level cloud amount and upper troposphere relative humidity calculated from the CRM cloud condensates and water vapor without a simulator (bottom). The blue dashed lines in the bottom two panels are the surface precipitation rate observed by TRMM precipitation radar.

	Satellite		MMF IR Simulator		MMF Actual		TRMM PR	
	Ocean	Land	Ocean	Land	Ocean	Land	Ocean	Land
PI (mm/day)	**0.5**	**1.8**	**3.6**	**2.0**	**0.25**	**0.25**	**0.43**	**0.61**
	[19%]	[51%]	[26%]	[17%]	[7.0%]	[10%]	[16%]	[24%]
	2.7	3.5	14.0	11.4	3.6	2.5	2.7	2.5
CLD (percent)	**1.0**	**3.8**	**0.5**	**1.9**	**0.7**	**2.0**		
	[8.7%]	[26.4%]	[2.4%]	[9%]	[2.7%]	[8.4%]		
	11.1	14.5	21.1	20.8	24.4	24.4		
UTH (percent)	**1**	**2.3**	**0.4**	**0.9**	**0.7**	**1.2**		
	[2.9%]	[6.3%]	[1%]	[2.4%]	[1.9%]	[3.2%]		
	33.5	36.2	35.9	36.2	36.1	38.5		

Table 2. July 1999 diurnal cycle statistics: bold text (first row in each cell) shows diurnal amplitude spatially-weighted averaged over tropical ocean and land respectively; percentage in brackets is the normalized diurnal amplitude by dividing the diurnal amplitude by the daily mean value; plain text (last row in each cell) is for daily means.

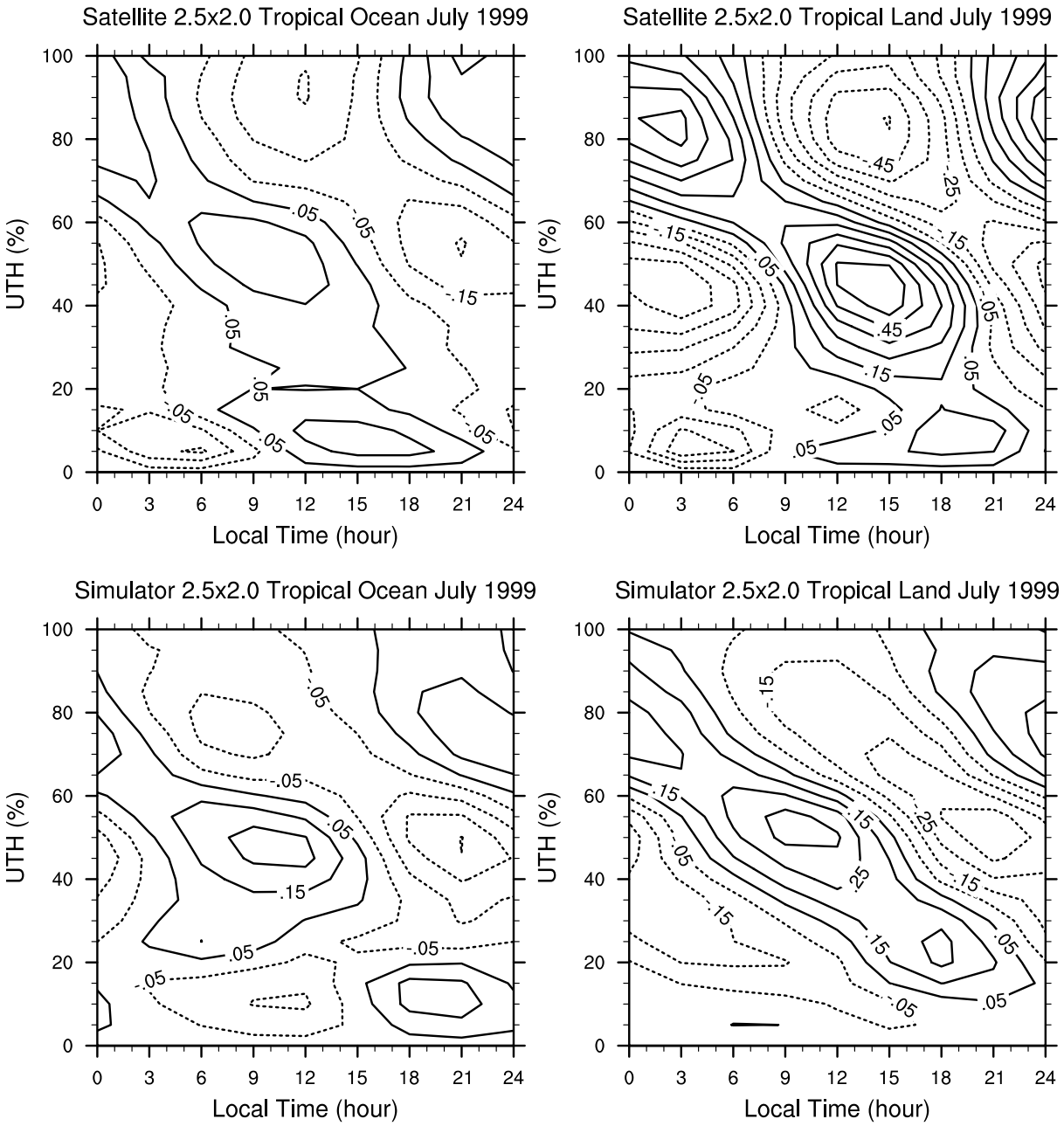

Figure 4. Histogram of the probability anomalies (in percent) for UTH to occur in each 5% bin at certain local standard time in July 1999. Top (bottom) panels are from geo-stationary satellite data (the infrared T_b simulator applied to the MMF) at resolution of 2.5^o longitude by 2^o latitude. Left (right) columns are for tropical ocean (land). The negative contour values are in dashed lines.

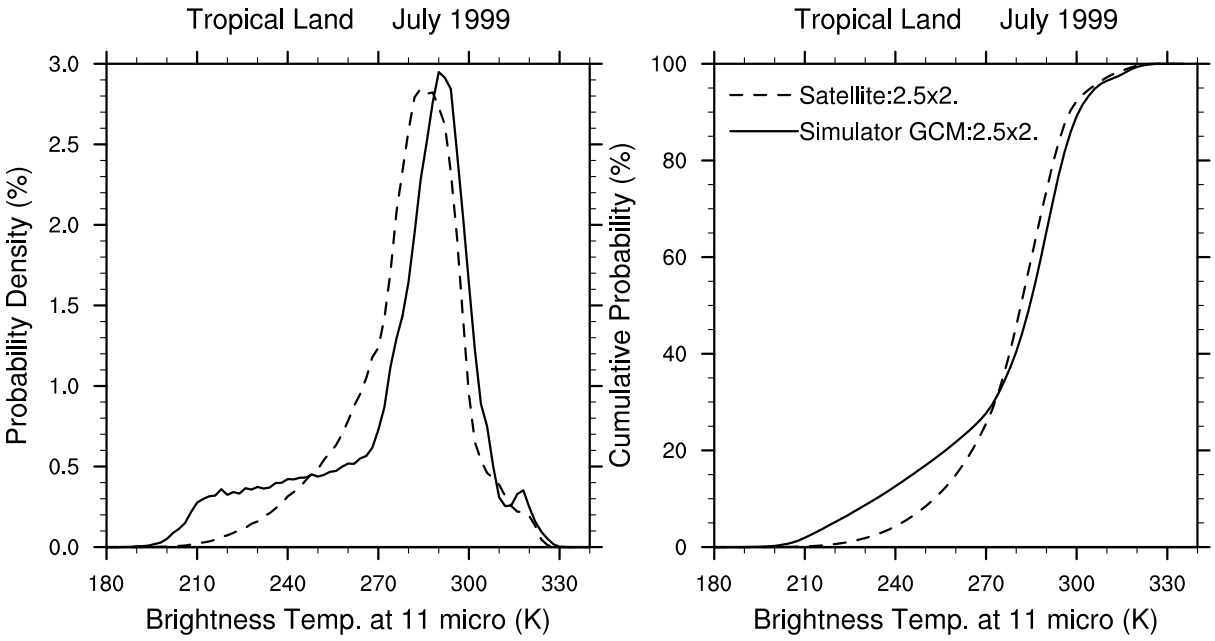

Figure 5. The probability density function (left) and cumulative probability (right) for the brightness temperatures at 11 micrometer, T_{11}, over land regions between 30^oS and 30^oN in July 1999. Dashed (solid) line is from geo-stationary satellite data (the IR T_b simulator applied to the MMF) at resolution of 2.5^o longitude by 2^o latitude.

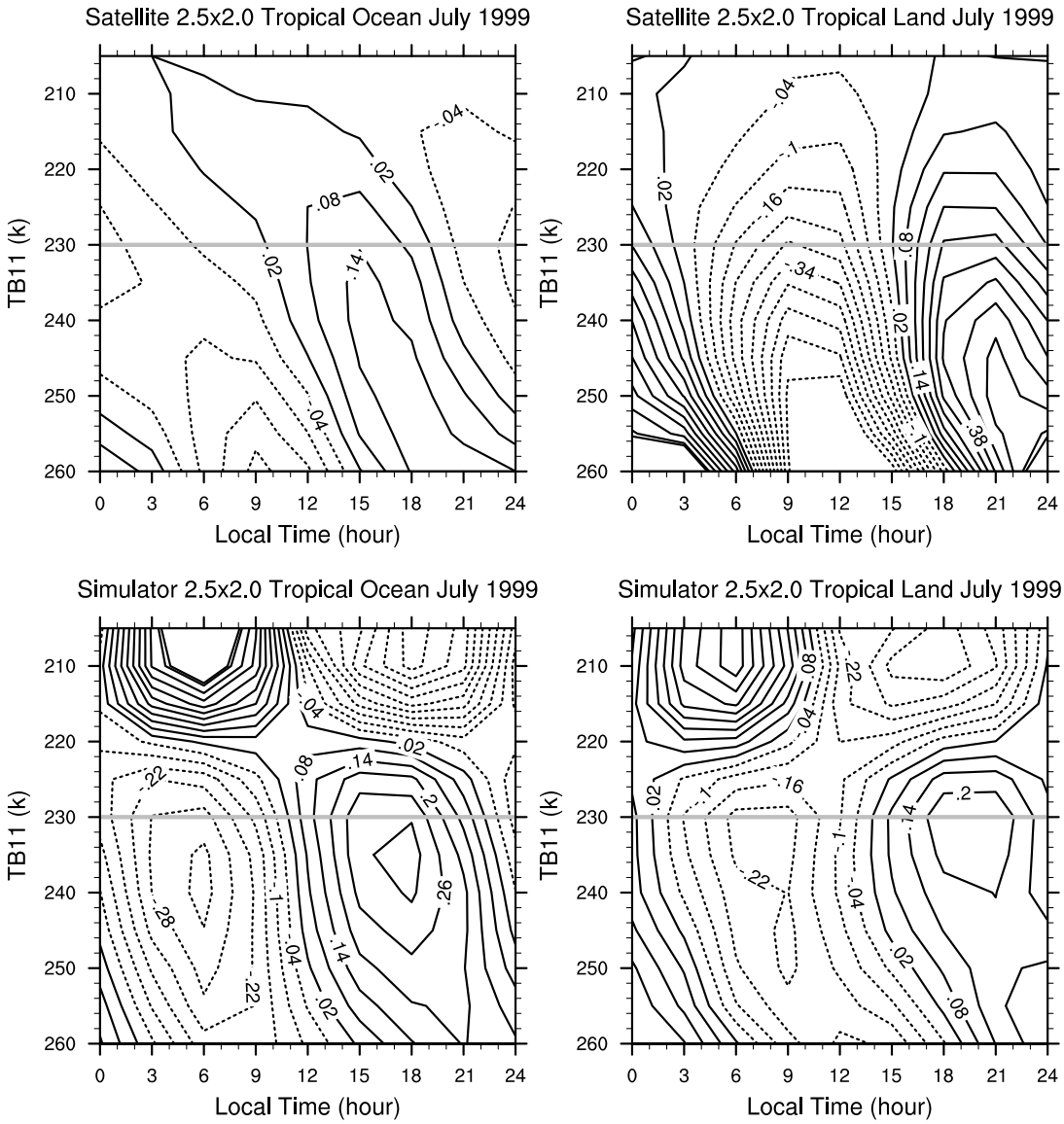

Figure 6. Histogram of the probability anomalies (in percent) for T_{11} to occur in each 5 k bin at certain local standard time in July 1999. Top (bottom) panels are from geo-stationary satellite data (the infrared T_b simulator applied to the MMF) at resolution of 2.5^o longitude by 2^o latitude. Left (right) columns are for tropical ocean (land). The negative contour values are in dashed lines. The gray line is the 230 K threshold to distinguish deep convective clouds (DCC) and convective anvil clouds (CAC).

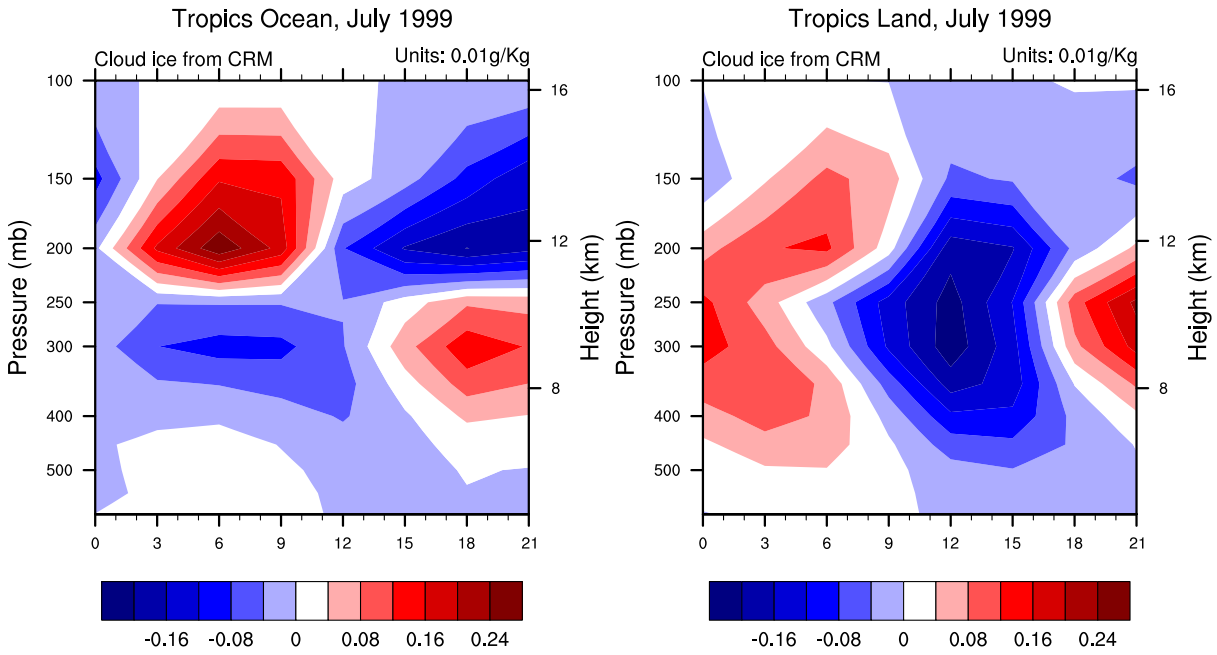

Figure 7. Land-sea composites for diurnal anomalies of GCM-grid-box-mean cloud ice at levels above 600 hPa. Units: 0.01g/kg

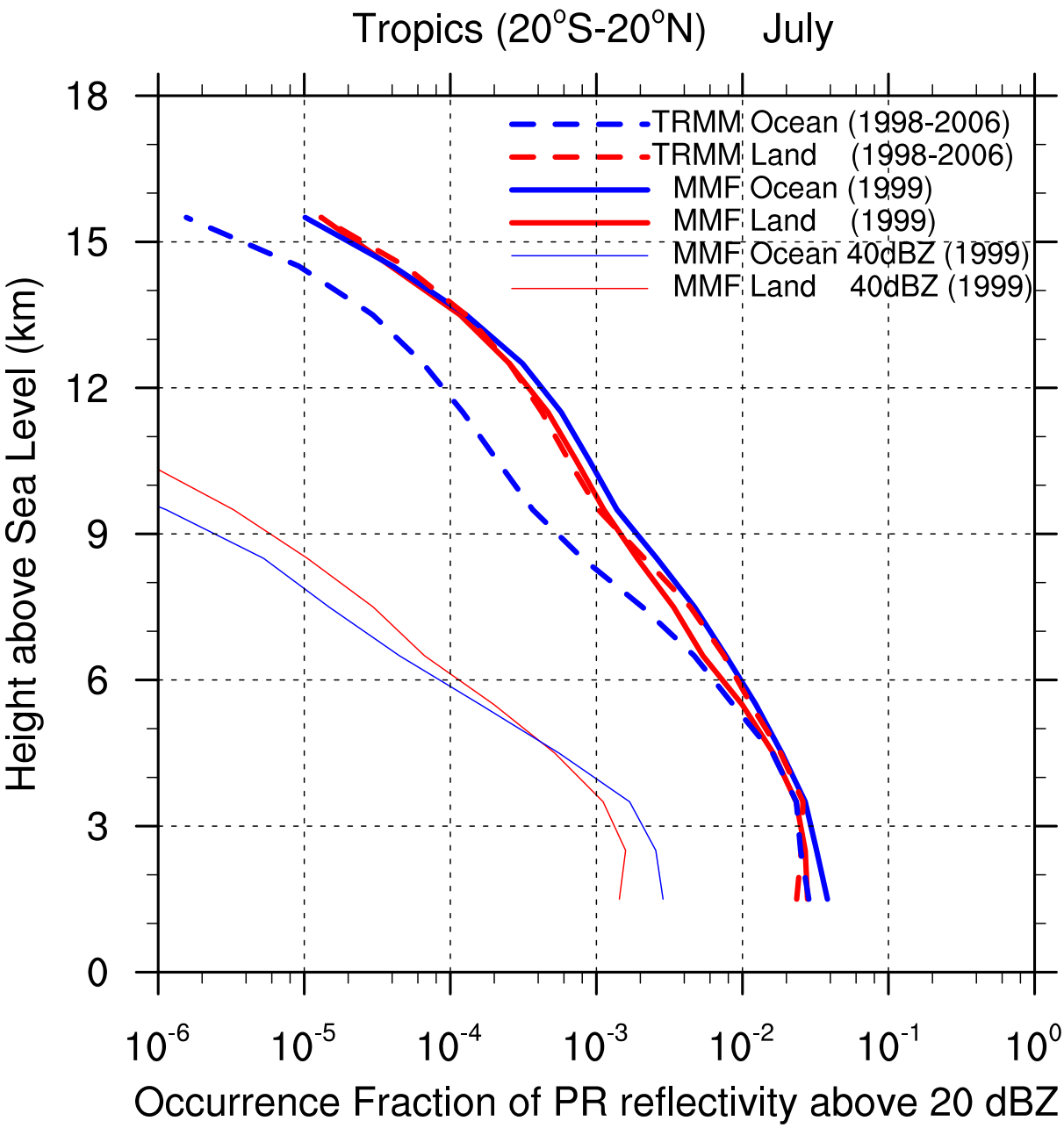

Figure 8. The occurrence fraction of precipitation radar (PR) reflectivity $\geqslant$ 20 dBZ in July in tropics (20^{o}S-20^{o}N). Blue (red) lines are for tropical ocean (land). Solid lines are from the PR simulator applied to the MMF CRM data in July 1999. Dashed lines are from the TRMM PR data in July averaged over the years 1998 to 2006. The MMF July 1999 40 dBZ or greater occurrence fractions are shown in thin lines. Note that the X-axis is in logarithmic scale.

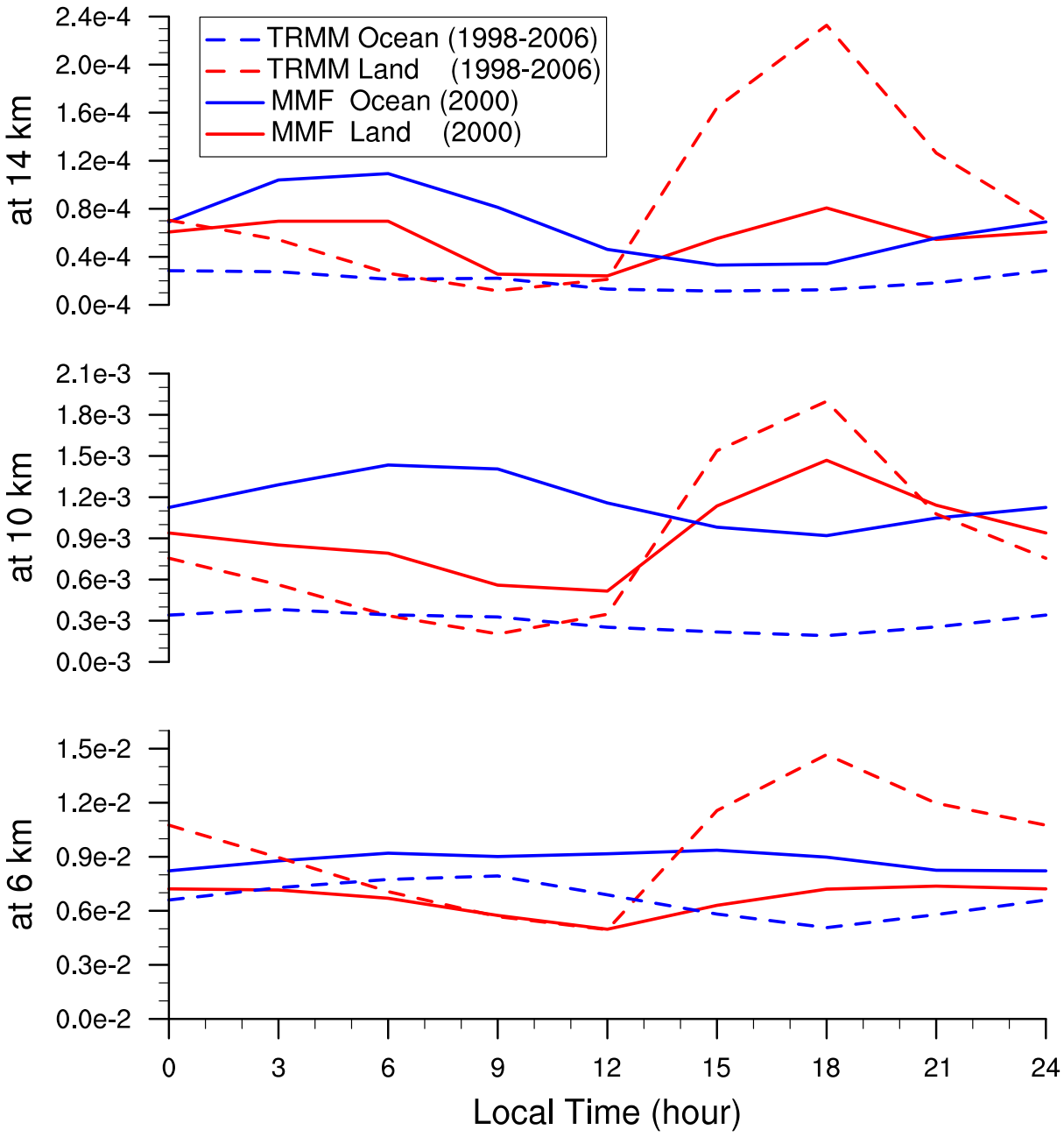

Figure 9. Diurnal cycle of the 20 dBZ or greater precipitation radar (PR) reflectivity occurrence fraction in July in 20°S-20°N at three height levels: 14 km (top), 10 km (middle) and 6 km (bottom). Blue (red) lines are for tropical ocean (land). Solid lines are from the PR simulator applied to the MMF CRM data in July, 1999. Dashed lines are from the TRMM PR data in July averaged in years 1998 to 2006.

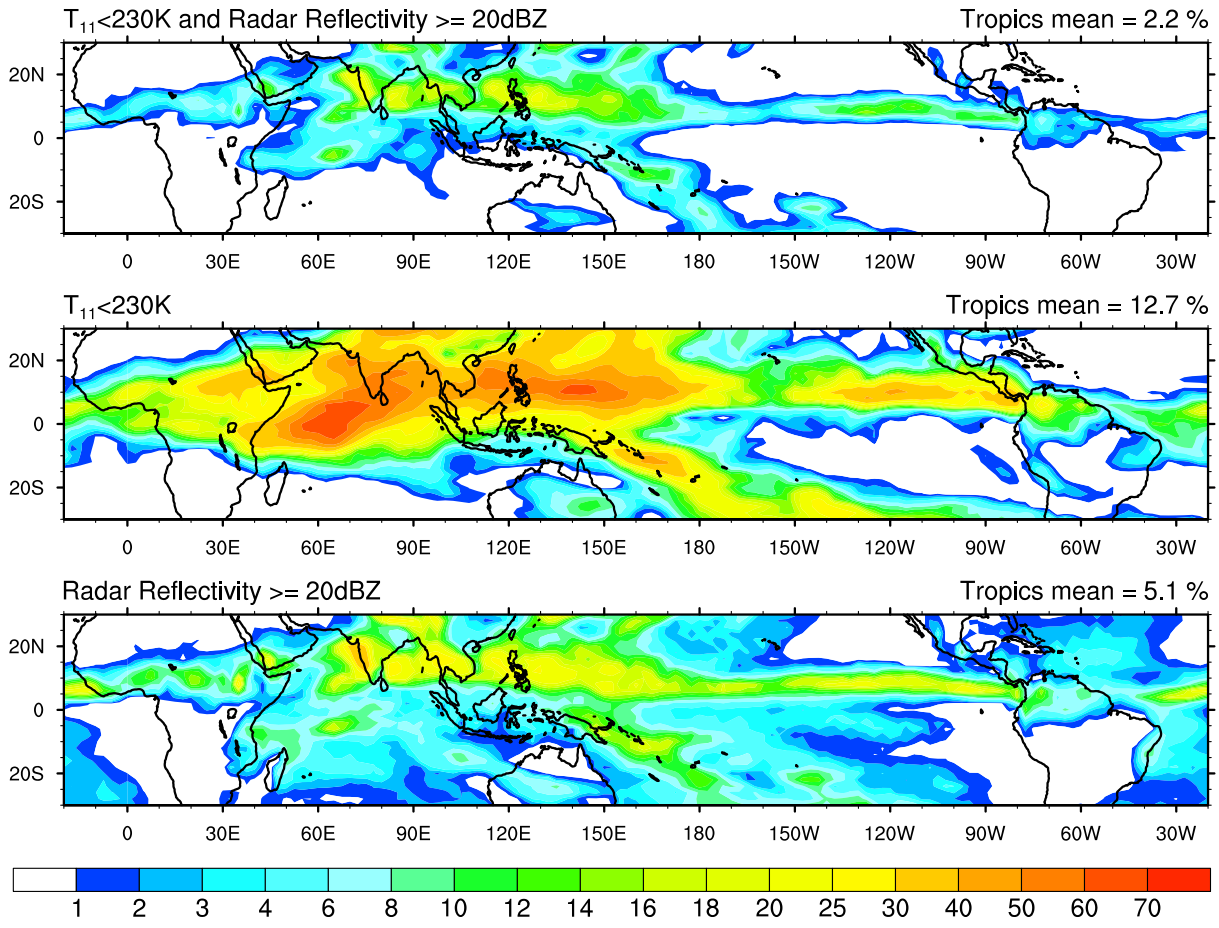

Figure 10. July 1999 daily mean probability (in percent) for simulators to detect CRM columns at each GCM grid box in the MMF: with IR $T_{11} < 230$ K and PR reflectivity $\geqslant$ 20dBZ (top); with IR $T_{11} < 230$ K only (middle); with PR reflectivity $\geqslant$ 20dBZ only (bottom).

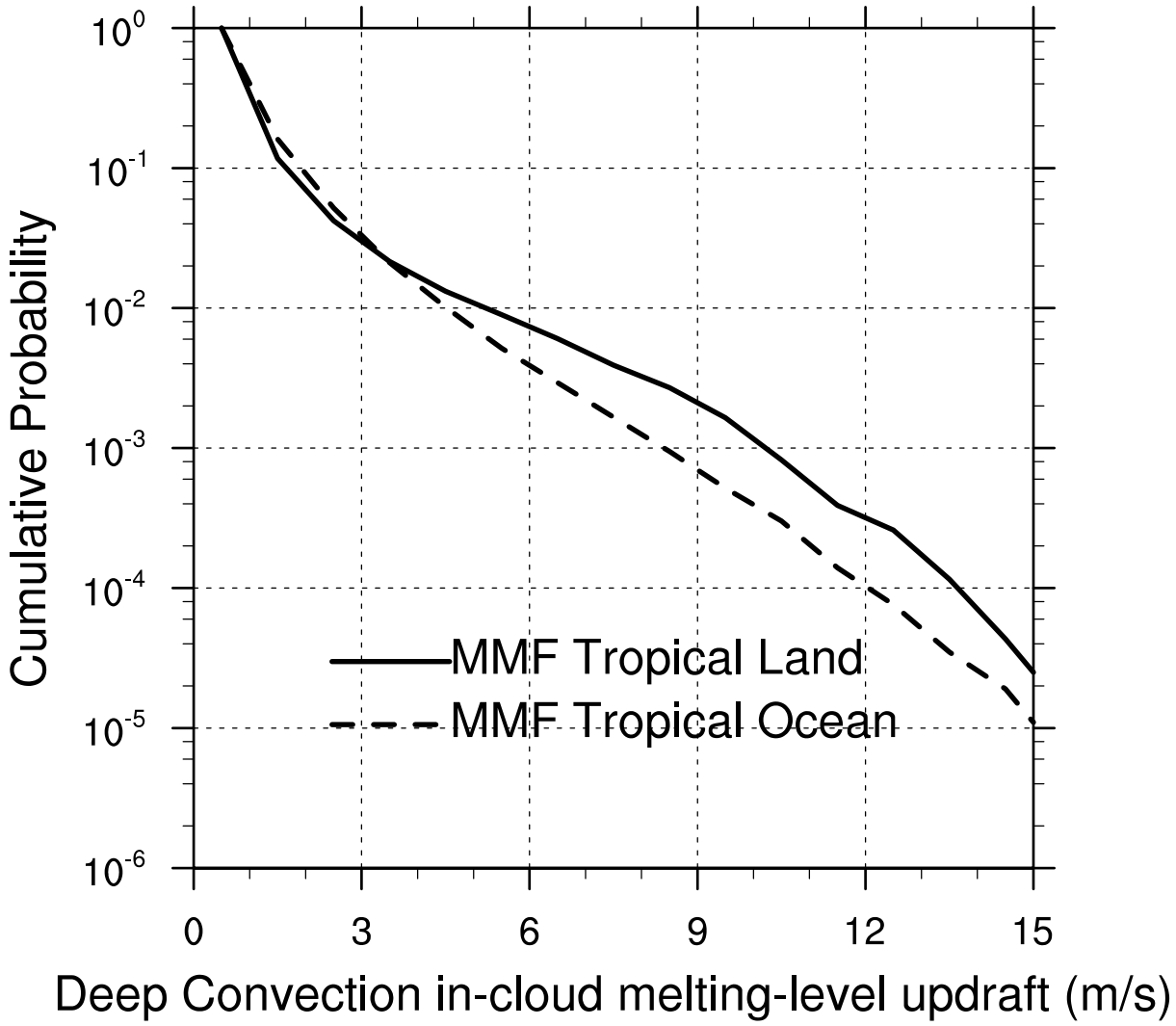

Figure 11. The cumulative probability of deep-convection in-cloud melting-level updraft in July 2000, dashed line for ocean and solid line for land.

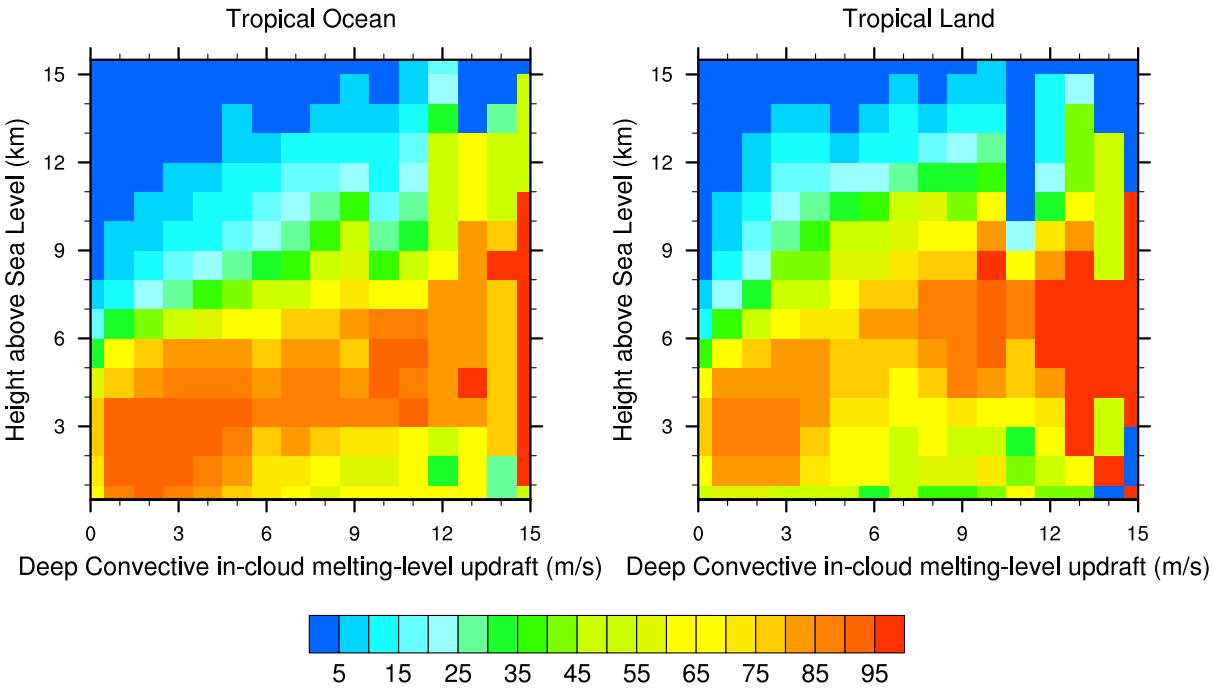

Figure 12. The probability (in percent) for PR reflectivity of 20 dBZ or greater to occur at a given height in each 1 m/s bin of deep-convective in-cloud melting-level updrafts in July 2000.

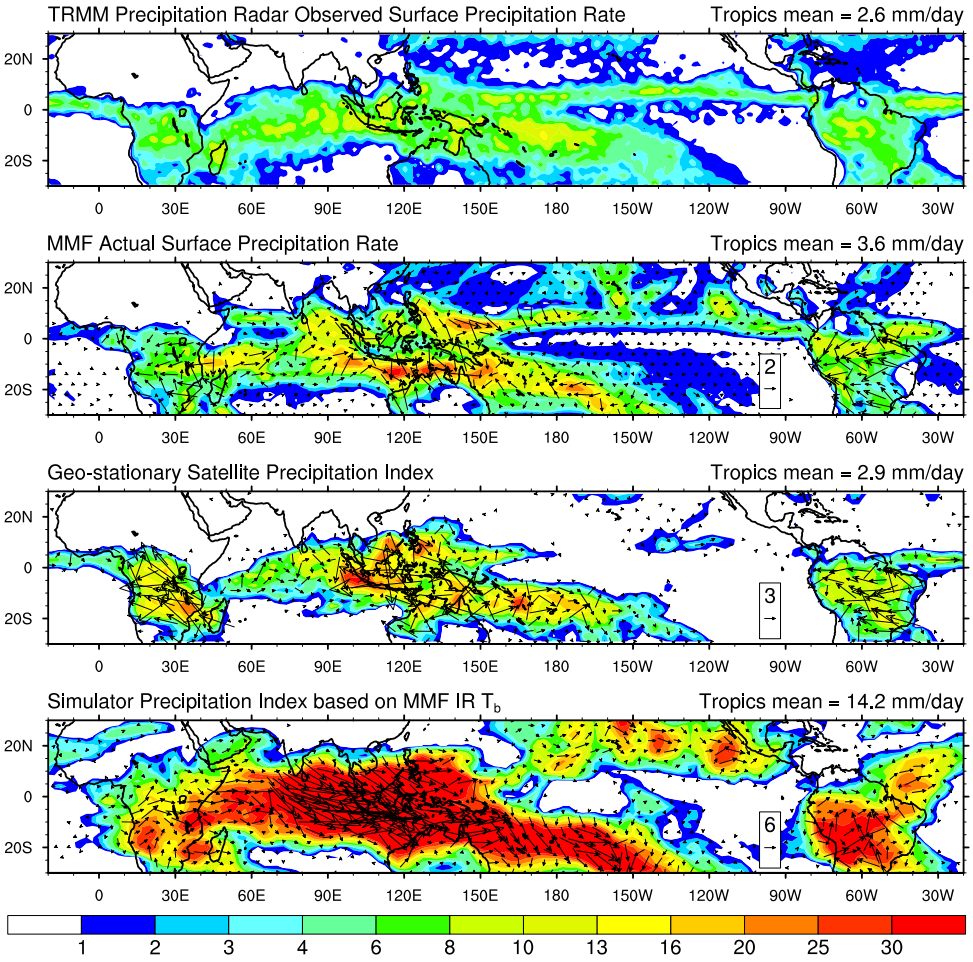

Figure 13. Maps of daily means and the monthly mean diurnal cycles: surface precipitation rate from TRMM precipitation radar in January averaged over years 1998 to 2006 (top); the MMF actual surface precipitation rate in January 2000 (second); precipitation index (PI) from geo-stationary satellite in January 1999 (third); PI from the IR T_b simulator applied to the MMF in January 2000 (bottom). Same legends as in Figure 2.

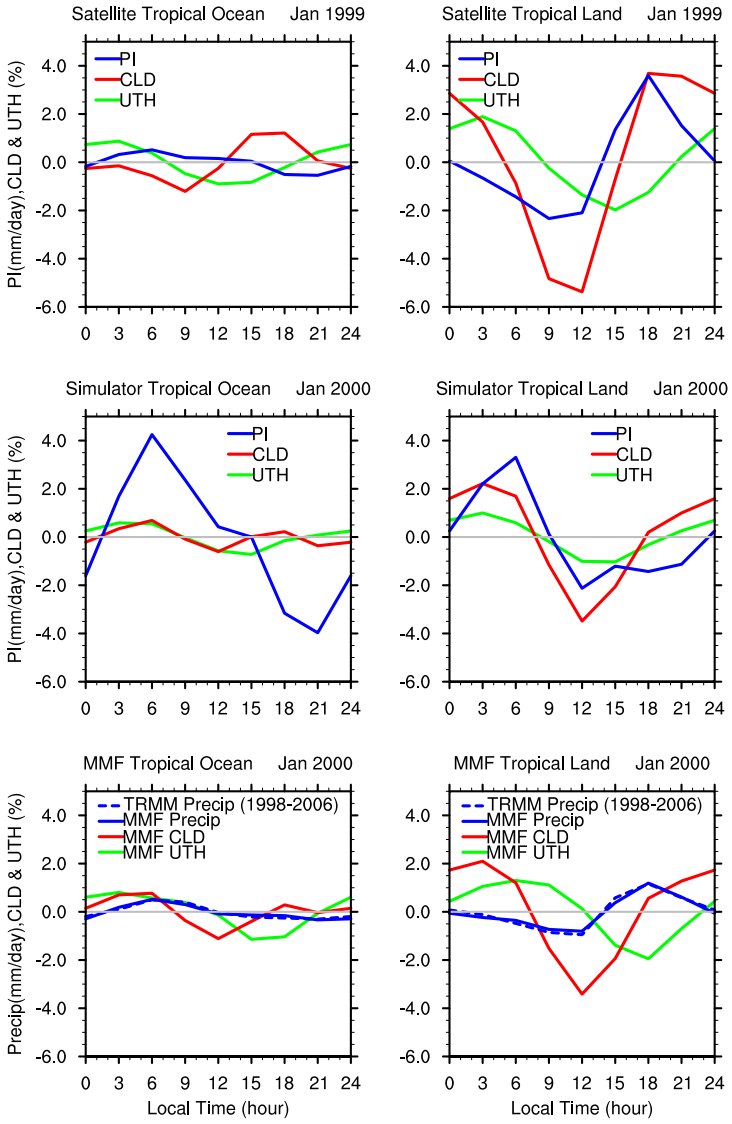

Figure 14. Same as in Figure 3 but for January.

	Satellite		MMF IR Simulator		MMF Actual		TRMM PR	
	Ocean	Land	Ocean	Land	Ocean	Land	Ocean	Land
	0.46	**2.45**	**3.5**	**2.2**	**0.35**	**0.8**	**0.39**	**0.88**
PI (mm/day)	[19%]	[60%]	[24%]	[17%]	[9.1%]	[28%]	[14%]	[36%]
	2.5	4.1	14.6	12.8	3.9	2.9	2.7	2.4
	0.9	**4.5**	**0.25**	**2.5**	**0.6**	**2.5**		
CLD (percent)	[7.8%]	[26%]	[1.1%]	[11%]	[2.4%]	[9.2%]		
	11.5	17.2	22.7	23.7	25.8	27.4		
	0.9	**1.9**	**0.6**	**1.0**	**0.9**	**1.6**		
UTH (percent)	[2.7%]	[4.9%]	[1.5%]	[2.5%]	[2.4%]	[3.9%]		
	33.4	38.7	40.7	40.7	39.0	40.2		

Table 3. As in Table 2 but for January.

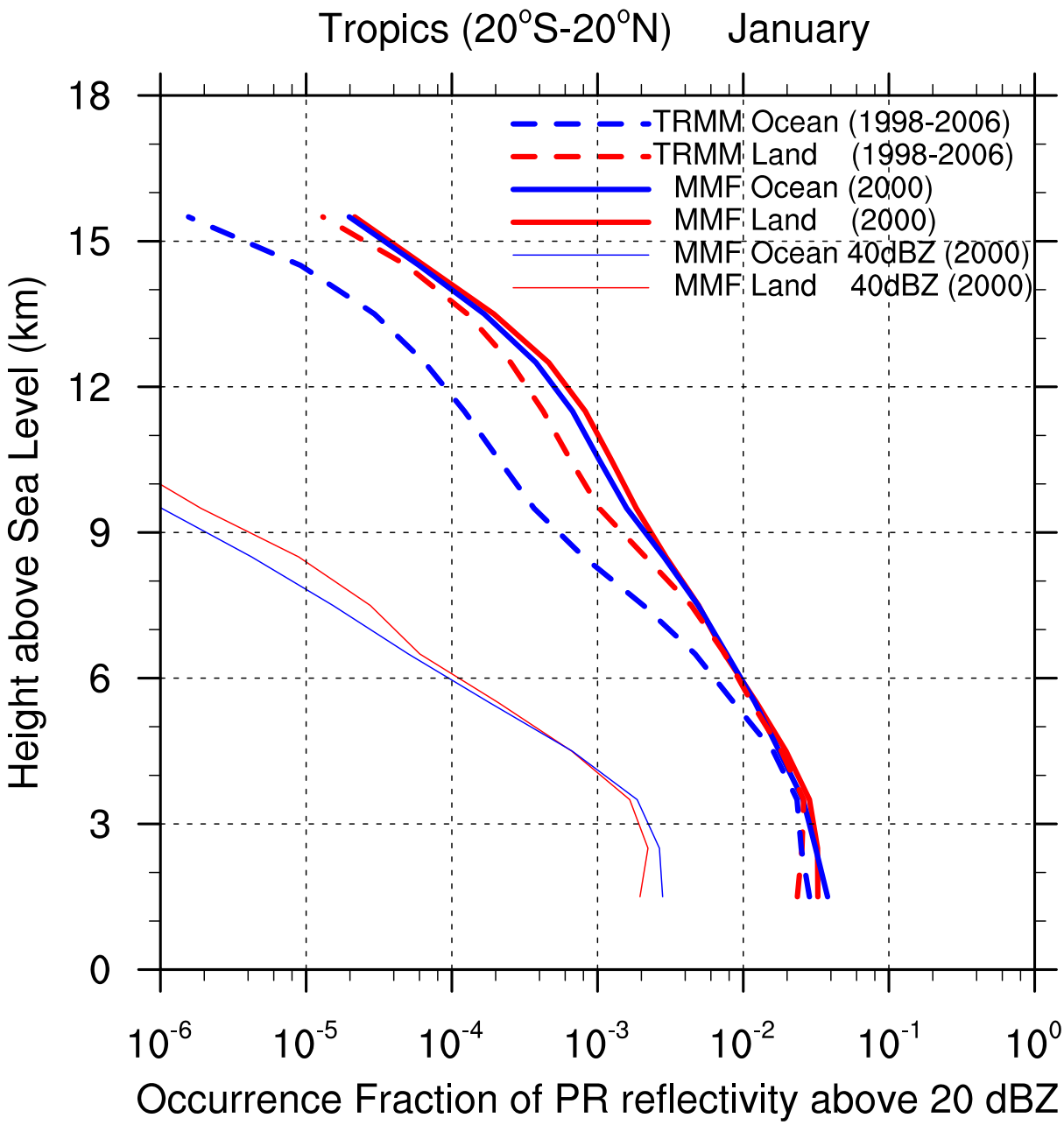

Figure 15. Same as in Figure 8, but for January.

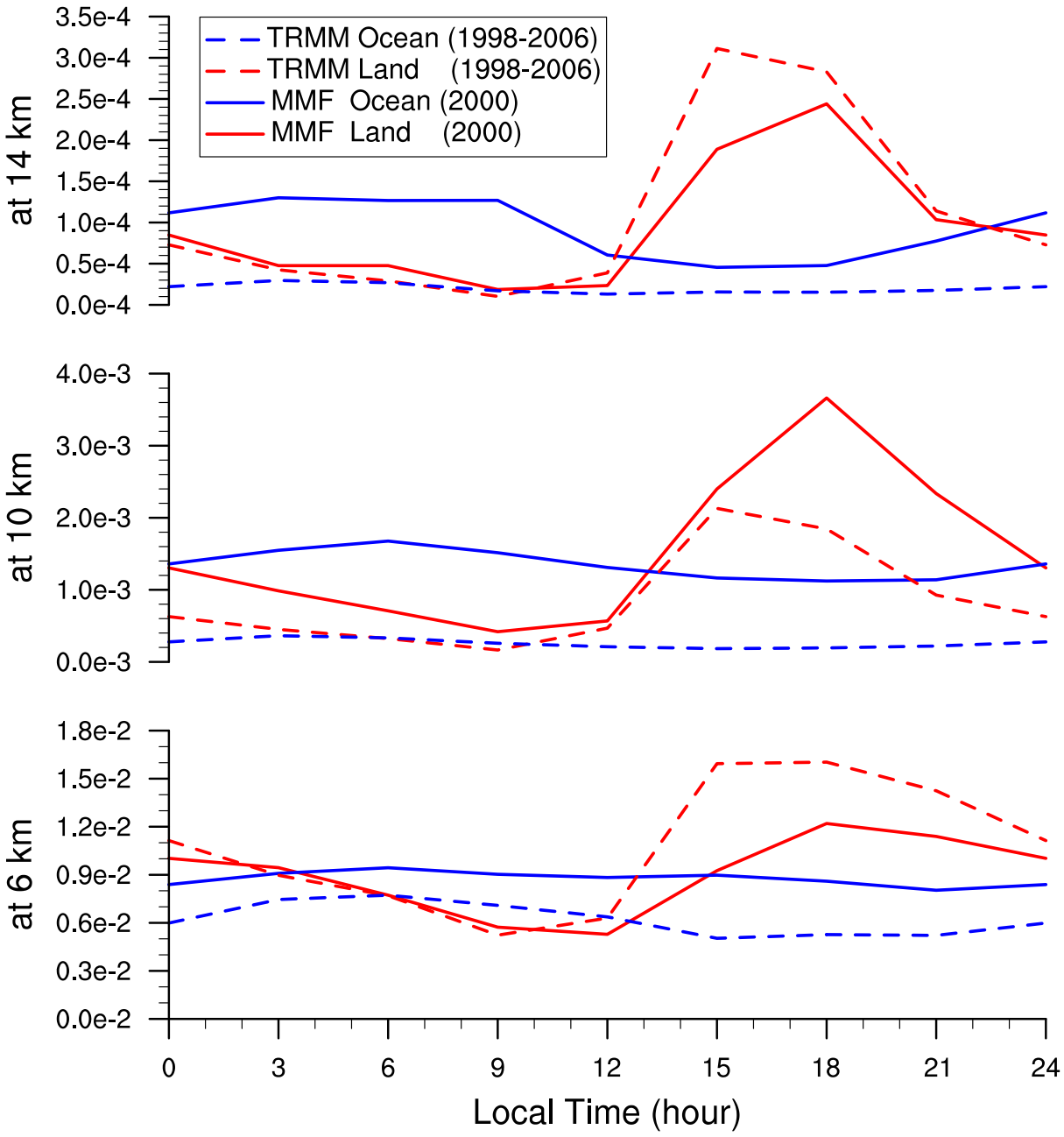

Figure 16. Same as in Figure 9, but for January.